GEOPHYSICS, VOL. 78, NO. 1 (JANUARY-FEBRUARY 2013); P. E1–E17, 17 FIGS.
10.1190/GEO2011-0520.1

Decomposition in upgoing and downgoing fields and inversion of marine CSEM data

Rune Mittet[1] and Pål Tunbrumo Gabrielsen[1]

ABSTRACT

We describe a data-driven method to estimate the top-formation resistivity using marine controlled-source electromagnetic data. The procedure exploits the fact that the airwave contributions are traveling up or down with a Poynting vector close to the vertical axis. The proposed method is based on forming an impedance in the same way as it is done in magnetotelluric processing. The top-formation resistivity is used to perform up-down decomposition of the electric field below the seabed. This procedure suppresses the contribution from the airwave in the resulting upgoing electric field and increases the data sensitivity to the subsurface resistivity distribution. The upgoing electric field is used in the misfit kernel for an inversion scheme. This is a method that is intended for use in shallow water. Inversion using the upgoing electric field means that the observed electric and magnetic fields contribute to the data misfit. The optimization procedure seeks to reduce the misfit between the observed and predicted data for both fields. We compared this procedure with the conventional procedure of predicting electric fields only. The addition of magnetic data improved the resolution for the synthetic and the real data examples. We performed postinversion modeling on the final resistivity models. The weighted misfit of the electric data was added to the weighted misfit of the magnetic data to form the total error. We found that this total error was smallest for the case in which we used the upgoing electric field in the misfit kernel.

INTRODUCTION

Marine controlled-source electromagnetic (CSEM) methods for hydrocarbon reservoir detection have now been in commercial use for more than a decade (Eidesmo et al., 2002; Ellingsrud et al., 2002). The development of the marine CSEM method over the last 40 years with emphasis on the last 10 years is reviewed in Constable (2010). The experimental equipment has improved considerably over the last decade and so have the data processing methods. The dominating method for the processing of marine CSEM data today is full waveform inversion. It is straightforward to formulate and implement inversion schemes that use the electric and magnetic data acquired in a marine CSEM survey. However, there has been a preference for using only electric data for real case examples. One reason for this choice may be that in the past, magnetic data have had a slightly smaller dynamic range than electric data and the noise effects have been slightly larger for the magnetic data compared with the electric data. This is no longer the case. The quality of electric and magnetic data is today comparable over offset ranges used in the processing of marine CSEM data. One important driver for this harmonization between electric and magnetic channels is the fact that magnetotelluric (MT) impedance tensors can be extracted from the recorded electric and magnetic data using time intervals in which the transmitter is idle. Processing these MT data is an increasing trend. A second driver is that up-down decomposition of active source data (Amundsen et al., 2006) requires electric and magnetic data of equally good quality.

Key (2009) discusses separate and combined inversion of horizontal electric and magnetic data channels for a 1D resistivity distribution. His conclusion is that horizontal electric and magnetic channels performed equally well in separate inversions and that there was no improvement or degradation of the recovered resistivity models by combining them in simultaneous inversion. Ou et al. (2011) do similar tests allowing for a 3D resistivity distribution. One of their findings is that inversion results may improve by also including the magnetic data in the optimization procedure. This is an indication that magnetic measurements are not always redundant in the marine CSEM case. The difference in opinion with regard to the effect of including magnetic fields between Key (2009) and Ou et al. (2011) may be model dependent and can, e.g., be related to the difference in the assumed resistivity distribution (1D versus 3D).

Manuscript received by the Editor 23 December 2011; revised manuscript received 2 August 2012; published online 10 December 2012.
[1]EMGS ASA, Trondheim, Norway. E-mail: rm@emgs.com; ptg@emgs.com.

The focus of this paper is on the processing of data acquired in water depths less than 500 m where there is a substantial airwave contribution. Our approach is similar to Key (2009) and Ou et al. (2011) because we use electric and magnetic data. The difference is that we use the magnetic data to perform up-down decomposition (Amundsen et al., 2006) of the observed and predicted data. The reduction in the misfit between observed and predicted magnetic data will be an implicit effect. This choice of optimization strategy is based on the fact that for shallow-water surveys, there is a large contribution to the horizontal electric and magnetic fields due to the airwave, which can be suppressed by extracting the upgoing field. The MT contribution in the upgoing electric field can also be assumed to be much smaller than for the total electric field. Properties of the airwave, including the importance of considering multiple scattering events in the seawater, are discussed by Nordskag and Amundsen (2007) and Andréis and MacGregor (2008). One concern with regard to the airwave has been that a response from a resistive thin hydrocarbon bearing layer can be hard to detect in the background of a large airwave contribution when the transmitted waveform is a harmonic. Thus, 10 years ago the view was that the marine CSEM method had problems in water depths of 500 m or less. This has turned out to be a conservative estimate.

It was clear by 2003 that marine CSEM could be applied with success in water depths of 300 m. Work with synthetic data indicated that frequency-domain marine CSEM combined with up-down decomposition gave sufficient sensitivity to a buried resistor at these water depths. This was part of the motivation for the first calibration survey on the Troll Western Gas province in 2003 (Johansen et al., 2005). In fact, it turned out that the response from the reservoir was so strong that up-down decomposition was not necessary to detect the reservoir. But, as demonstrated in Amundsen et al. (2006), the up-down decomposition enhanced the sensitivity to the hydrocarbon charged reservoir significantly.

EMGS conducted a combined research and commercial survey in 2006 in 60 m of water depth in the southern part of the Norwegian sea. This data set was processed by a then recently developed CMP inversion algorithm (Mittet et al., 2008) as a test. A resistive object was identified, but it did not coincide with the seismic target, which was a four-way closure. No well was drilled. However, the inversion results looked reasonable and consistent. More work on synthetic data was required to see if marine CSEM could be trusted at these water depths. Some of the results from this work are presented in Mittet (2008).

The concluding answer in Mittet (2008) is that frequency-domain marine CSEM can work in very shallow water, that is, down to 40 m or even less. Mittet (2008) points to the fact that proper phase measurements are essential. Normalized amplitudes in the standard fashion in which the absolute value of the electric field is normalized on corresponding data from a reference receiver do not work properly in shallow water. Taking absolute values in this manner discards phase information. As a remedy, a revised normalization expression, very similar to the kernel of a misfit functional used for inversion, was proposed. This expression took phase information into consideration and was shown to work for water depths of 40 m. A second finding in Mittet (2008) is that the amplitude of the scattered field from a buried resistor increases as the water depth is reduced. The increased amplitude of the scattered field compensates for the increase in airwave amplitude as the water depth is decreased. The scattered field is not dwarfed by the airwave in shallow water. This effect makes marine CSEM feasible in water depths of 40 m or less. The sensitivity to a buried resistor for data acquired in shallow water was further enhanced by performing up-down decomposition before application of the revised normalization procedure.

It is necessary that the up-down decomposition is performed below the seabed to significantly increase the sensitivity to the formation. This poses a problem because the top-formation horizontal resistivity, which must be known for up-down decomposition below the seabed, is not a standard measurement in a marine CSEM survey. One of the two topics in this paper is how a usable estimate of the top-formation resistivity can be performed in the absence of a direct resistivity measurement. The second topic is how to use the resulting upgoing electric field in inversion.

The inversion strategy proposed here is to first estimate the top-formation resistivity at the receiver location and use this value to calculate the characteristic impedance required for up-down decomposition. This characteristic impedance value is used unaltered throughout the inversion. The alternative is to extract the top-formation resistivity from the resistivity model at the current iteration. In this case, the top-formation resistivity and hence the characteristic impedance may change with the iterations. There are two reasons for our choice of strategy. The first reason is that we use a pixel-based representation of the conductivity/resistivity model for our inversion scheme. The most sensitive parts of the model are in this case close to the receiver locations. This is beneficial with respect to recovering the properties close to the receiver, but the downside is that noise and effects in the observed data that are not described properly by the forward model tend to force false updates in this part to reduce the overall misfit. The result may be an undesired receiver footprint in the conductivity/resistivity model. The use of such a footprint resistivity value to calculate the characteristic impedance can lead to a suboptimal up-down decomposition. By performing an estimate of the top-formation resistivity prior to inversion, we avoid any stability problems related to this footprint effect. The second reason for choosing this strategy is purely pragmatic. The inversion scheme we use for standard processing of electric data requires a minimum of modifications to adapt to the modified inversion kernel with upgoing fields.

THEORY

General expressions for up-down decomposition in a plane layered earth are given in Amundsen et al. (2006). These expressions cover situations in which the electromagnetic fields may propagate at any angle with respect to the vertical axis. Amundsen et al. (2006) and Nordskag and Amundsen (2007) demonstrate that the airwave can be approximated by a vertically propagating electromagnetic field assuming small lateral resistivity variations in the top formation. These are also the assumptions used here for the estimation of the top-formation resistivity. The upgoing electric field E_x^U and the downgoing electric field E_x^D are for vertical propagation given by Amundsen et al. (2006) as

$$E_x^U(\mathbf{x}_r,\omega|\mathbf{x}_s) = \frac{1}{2}\left(E_x(\mathbf{x}_r,\omega|\mathbf{x}_s) - Z_a H_y(\mathbf{x}_r,\omega|\mathbf{x}_s)\right),$$
$$E_x^D(\mathbf{x}_r,\omega|\mathbf{x}_s) = \frac{1}{2}\left(E_x(\mathbf{x}_r,\omega|\mathbf{x}_s) + Z_a H_y(\mathbf{x}_r,\omega|\mathbf{x}_s)\right), \quad (1)$$

where we have assumed an inline configuration. Here, $E_x(\mathbf{x}_r,\omega|\mathbf{x}_s)$ and $H_y(\mathbf{x}_r,\omega|\mathbf{x}_s)$ are the measured electric and magnetic fields,

respectively. The arguments $\mathbf{x}_r$, $\mathbf{x}_s$, and ω are receiver coordinate, source coordinate, and angular frequency, respectively. Z_a is the characteristic impedance for medium a, where in the following we will use Z_w for the seawater immediately above the seabed and Z_f for the top formation immediately below the seabed. The characteristic impedance is

$$Z_a = \sqrt{-i\mu_0\omega\rho_a}, \tag{2}$$

where μ_0 is the magnetic permeability and ρ_a is the resistivity of medium a. The characteristic impedance will be determined by the horizontal resistivity in the case of a transverse isotropic vertical (TIV) medium and vertically propagating fields. This is explained in Appendix A.

The electric and magnetic fields in equation 1 are measured at the boundary between the sea water and top formation. The fields are continuous over that boundary, so we are left with a choice for the characteristic impedance. It is the upgoing field that is of interest because this part of the field carries information that is required to reconstruct the subsurface. The seawater resistivity is logged during a marine CSEM survey, thus the characteristic impedance for seawater is immediately available. However, the upgoing field above the seabed has two components, namely, the part we seek, which is the upgoing field from the subsurface, but in addition, the reflection of the downgoing field at the seawater-formation boundary. The downgoing field in shallow water and at large offsets is dominated by the airwave. The reflection coefficient at the seawater-formation boundary is relatively large due to the large resistivity change at this interface, and this may give a situation in which the upgoing field above the seabed has a large airwave component. This component is avoided by doing up-down decomposition below the seabed where the only upgoing component is the upgoing field from the deeper part of the subsurface. Therefore, doing up-down decomposition below the seabed is the best choice. The problem is that we need the characteristic impedance Z_f or equivalently the resistivity ρ_f of the top formation to extract this component. The resistivity of the top formation is not logged during a marine CSEM survey. However, as we will demonstrate below, the resistivity of the top formation can be estimated, and this is important for our choice of inversion strategy for up-down decomposed data.

Inversion of up-down decomposed data

We use a finite-difference solver for this inversion scheme. The forward modeling is performed in a fictitious time domain (Lee et al., 1989; Maaø, 2007; Mittet, 2010). The fields are converted to the real frequency domain on the fly. The fictitious time domain method is effectively a multifrequency modeling scheme in which all frequencies of interest for a given source location (predicted state) or receiver location (adjoint state) can be extracted from one forward modeling. The scheme is 2.5D, and the wavenumber normal to the survey line (k_y) is implicit for most of the equations below. The term 2.5D covers 3D fields in a conductivity model that is invariant normal to the survey direction (2D conductivity model variations). The data part of the misfit is

$$\epsilon^D(\sigma_a^n) = \sum_{\mathbf{x}_r,\omega,\mathbf{x}_s} W(\mathbf{x}_r,\omega|\mathbf{x}_s)[\Delta\tilde{E}_x^n(\mathbf{x}_r,\omega|\mathbf{x}_s;\sigma_a^n)]^\dagger \times [\Delta\tilde{E}_x^n(\mathbf{x}_r,\omega|\mathbf{x}_s;\sigma_a^n)], \tag{3}$$

where

$$\Delta\tilde{E}_x^n(\mathbf{x}_r,\omega|\mathbf{x}_s;\sigma_a^n) = \tilde{E}_x^{\mathrm{Obs}}(\mathbf{x}_r,\omega|\mathbf{x}_s) - \tilde{E}_x^n(\mathbf{x}_r,\omega|\mathbf{x}_s;\sigma_a^n), \tag{4}$$

and the conductivity model at iteration n is $\sigma_a^n = \sigma_a^n(\mathbf{x})$. The conductivity model is TIV, thus the inversion scheme will estimate horizontal and vertical conductivity. The index a can take on the values h for horizontal conductivity and v for vertical conductivity. The $W(\mathbf{x}_r,\omega|\mathbf{x}_s)$ is a weighting function that is determined by the uncertainty and noise in the observed data. The properties of the weighting function will be discussed below.

The electric fields $\tilde{E}_x$ can be either the total fields or the decomposed upgoing fields. For the observed fields, we have two cases

$$\tilde{E}_x^{\mathrm{Obs}}(\mathbf{x}_r,\omega|\mathbf{x}_s) = \begin{cases} E_x^{\mathrm{Obs}}(\mathbf{x}_r,\omega|\mathbf{x}_s) \\ \frac{1}{2}[E_x^{\mathrm{Obs}}(\mathbf{x}_r,\omega|\mathbf{x}_s) - Z_f H_y^{\mathrm{Obs}}(\mathbf{x}_r,\omega|\mathbf{x}_s)] \end{cases}, \tag{5}$$

where the upper expression is the total field and the lower expression is the upgoing field as given by equation 1. For the predicted fields at iteration n, we have

$$\tilde{E}_x^n(\mathbf{x}_r,\omega|\mathbf{x}_s;\sigma_a^n) = \begin{cases} E_x^n(\mathbf{x}_r,\omega|\mathbf{x}_s;\sigma_a^n) \\ \frac{1}{2}[E_x^n(\mathbf{x}_r,\omega|\mathbf{x}_s;\sigma_a^n) - Z_f H_y^n(\mathbf{x}_r,\omega|\mathbf{x}_s;\sigma_a^n)] \end{cases}. \tag{6}$$

The use of upgoing electric fields is one of several ways of including magnetic data in the inversion. The inclusion of magnetic fields in the inversion of marine CSEM data is discussed in Key (2009) and Ou et al. (2011). The formulation used here is specifically targeted toward shallow water cases. We note here that the plane wave approximation we use for the up-down decomposition is most accurate at intermediate and large offsets. This is also the offset domain where the weight function W gives the largest contribution to the misfit. However, the misfit function for the decomposed upgoing data still makes perfect sense at small offsets. Observed and predicted data are decomposed with the same Z_f, so at any offset this can be viewed as a particular weighting of electric relative to magnetic contributions. We may have a situation in which Z_f is poorly estimated. If the expressions for the upgoing fields in equations 5 and 6 are inserted in equation 3, we observe that the misfit will be at a minimum when the predicted electric field approximates the observed electric field and the predicted magnetic field approximate the observed magnetic field. This is a desired property. The contribution to the total misfit from the magnetic part relative to the electric part is determined by Z_f. A poorly estimated Z_f will not change the fact that it is the observed electric and the observed magnetic fields that are sought, predicted by the inversion. However, a poorly estimated Z_f may influence the final result because the value of Z_f determines how effective the airwave contributions are suppressed. The inversion of the "electric field data only" can be viewed as a limiting case of inverting upgoing electric fields in which the amplitude of Z_f is severely underestimated. We have also performed inversion using only magnetic data. Those results are similar to those using only electric data. Inversion of "magnetic data only" can be viewed as a limiting case in which the amplitude of Z_f is severely overestimated using upgoing electric fields. Our view is that a proper estimate of Z_f gives a good balance between electric and magnetic data contributions in the misfit functional and ensures

a proper airwave suppression at intermediate and large offsets. A poor estimate of Z_f will tip this balance either toward the domination by the electric contribution or toward the domination by the magnetic contribution. The characteristic impedance has a fixed phase of $-\pi/4$ independent of the resistivity. A poorly estimated top formation resistivity cannot change this phase. It is the relative weight between the electric contribution and the magnetic contribution to the misfit functional that change with the top-formation resistivity estimate. This ensures stability for inversion of upgoing electric fields. The two limiting cases for an extremely poor estimate of the top-formation resistivity are inversion of electric data only or inversion of magnetic data only, depending on whether the characteristic impedance is underestimated or overestimated. We know that these two extreme cases give inversion results that are acceptable. However, to achieve improvements, we need a reasonably good estimate of the top-formation resistivity. What we hope for is that a top-formation resistivity estimate that is in error by some percentage still can give an effective up-down decomposition. This will be demonstrated and quantified by the real data examples that follow.

The Fréchet derivatives are

$$\tilde{\mathcal{F}}_x^n(\mathbf{x}_r,\omega|\mathbf{x}_s;\mathbf{x}) = \begin{cases} \partial_{\sigma_a^n} E_x^n(\mathbf{x}_r,\omega|\mathbf{x}_s;\sigma_a^n) \\ \frac{1}{2}[\partial_{\sigma_a^n} E_x^n(\mathbf{x}_r,\omega|\mathbf{x}_s;\sigma_a^n) - Z_f \partial_{\sigma_a^n} H_y^n(\mathbf{x}_r,\omega|\mathbf{x}_s;\sigma_a^n)] \end{cases}. \quad (7)$$

The Fréchet derivatives are calculated in the Born approximation using forward modeling from source and receiver locations (Abubakar et al., 2008). Let G_{ij}^{EJ} denote the electric Green's function in the i direction due to an electric dipole source in the j direction and G_{ij}^{EK} denote the electric Green's function in the i direction due to an magnetic dipole source in the j direction. As an example, for the Fréchet derivatives with respect to vertical resistivity, we have

$$\begin{aligned} &\partial_{\sigma_v^n} E_x^n(\mathbf{x}_r,\omega|\mathbf{x}_s;\sigma_a^n) \\ &\quad = \Delta V(\mathbf{x}) \frac{1}{\pi} \int_0^{K_m} dk_y G_{zx}^{EJ}(\mathbf{x},k_y|\mathbf{x}_r) G_{zx}^{EJ}(\mathbf{x},k_y|\mathbf{x}_s) J_x(\mathbf{x}_s), \\ &\partial_{\sigma_v^n} H_y^n(\mathbf{x}_r,\omega|\mathbf{x}_s;\sigma_a^n) \\ &\quad = -\Delta V(\mathbf{x}) \frac{1}{\pi} \int_0^{K_m} dk_y G_{zy}^{EK}(\mathbf{x},k_y|\mathbf{x}_r) G_{zx}^{EJ}(\mathbf{x},k_y|\mathbf{x}_s) J_x(\mathbf{x}_s), \end{aligned} \quad (8)$$

where $\Delta V(\mathbf{x})$ is the size of the variation, assuming it is small, and K_m is the maximum wavenumber in the crossline direction. The number of wavenumbers is normally between 15 and 20 with a logarithmic spacing. The additional numerical cost of calculating the magnetic Fréchet derivatives is small because the number of receiver-position Green's functions that must be calculated is an order of magnitude less than the number of source-position Green's functions that must be calculated. The source-position Green's functions are common to the expressions in equation 8.

We define the misfit as a function of the perturbation $\delta\sigma_a^n(\mathbf{x})$ as

$$\begin{aligned} \epsilon^D(\sigma_a^n + \delta\sigma_a^n) = \sum_{\mathbf{x}_r,\omega,\mathbf{x}_s} & W(\mathbf{x}_r,\omega|\mathbf{x}_s) \\ & \times (\Delta\tilde{E}_x^n(\mathbf{x}_r,\omega|\mathbf{x}_s;\sigma_a^n) - \delta\tilde{E}_x^n(\mathbf{x}_r,\omega|\mathbf{x}_s;\sigma_a^n))^\dagger \\ & \times (\Delta\tilde{E}_x^n(\mathbf{x}_r,\omega|\mathbf{x}_s;\sigma_a^n) - \delta\tilde{E}_x^n(\mathbf{x}_r,\omega|\mathbf{x}_s;\sigma_a^n)), \end{aligned} \quad (9)$$

where

$$\delta\tilde{E}_x^n(\mathbf{x}_r,\omega|\mathbf{x}_s;\sigma_a^n) = \tilde{\mathcal{F}}_x^n(\mathbf{x}_r,\omega|\mathbf{x}_s;\mathbf{x})\delta\sigma_a^n(\mathbf{x}), \quad (10)$$

and require stationarity with respect to a variation in $\delta\sigma_a^n(\mathbf{x})$. This gives the normal equations for the data-space part of the problem, which have the general form for an update $\Delta\sigma_a^n(\mathbf{x})$,

$$\begin{aligned} &\sum_{\mathbf{x}'} \sum_{\mathbf{x}_r,\omega,\mathbf{x}_s} \Delta V(\mathbf{x}')[\tilde{\mathcal{F}}_x^{n\dagger}(\mathbf{x}_r,\omega|\mathbf{x}_s;\mathbf{x}')W(\mathbf{x}_r,\omega|\mathbf{x}_s)\tilde{\mathcal{F}}_x^n(\mathbf{x}_r,\omega|\mathbf{x}_s;\mathbf{x})\Delta\sigma_a^n(\mathbf{x}') + c.c] \\ &\quad = \sum_{\mathbf{x}_r,\omega,\mathbf{x}_s} [\tilde{\mathcal{F}}_x^{n\dagger}(\mathbf{x}_r,\omega|\mathbf{x}_s;\mathbf{x})W(\mathbf{x}_r,\omega|\mathbf{x}_s)\Delta\tilde{E}_x^n(\mathbf{x}_r,\omega|\mathbf{x}_s;\sigma_a^n) + c.c]. \end{aligned} \quad (11)$$

The model-space misfit functional is

$$\epsilon^M(\sigma_a^n) = \lambda R(\sigma_a^n), \quad (12)$$

where λ is the Tikhonov parameter and $R(\sigma_a^n)$ is the regularization function. We have several model-space regularization functions available, ranging from smoothness constraints to soft constraints on the fit to seismic horizons (Hansen and Mittet, 2009). For the examples shown here, we use minimum horizontal gradient regularization. The model-space part is added to the data-space part, and the whole system is solved by a Gauss-Newton scheme.

The above formalism is suited for inversion of total electric data and upgoing electric data. The only challenge is that the inversion of upgoing electric data requires Z_f to be known. The top-formation resistivity can be extracted from the current inversion model, as is done by Roth and Zach (2007) for a 1D simulated annealing scheme. However, as already mentioned, the formation resistivity immediately below a receiver is sometimes hard to determine properly with a local inversion scheme. We have decided to use a fixed value for the characteristic impedance of the top formation. The estimation procedure for Z_f is our next topic.

Estimation of up-down decomposed data

As already mentioned, we assume vertically propagating fields for the up-down decomposition. Thus, it is possible to calculate an apparent resistivity from the electric and magnetic fields at the offsets in which this approximation is reasonable. This procedure is used in controlled source audio-frequency magnetotellurics (CSAMT) processing (Zonge and Hughes, 1991). Andréis et al. (2009) propose a similar scheme for marine CSEM data processing in which the large offset data are processed by conventional MT techniques with the purpose of improving structural imaging. We will adopt the same technique here, but with the purpose of estimating the top-formation resistivity. The necessary modifications for this particular application are discussed in Appendix B. There are two issues that are of particular interest. The first issue is the choice of the proper offset range, this is in common with the CSAMT (Zonge and Hughes, 1991) and the marine CSEM (Andréis et al., 2009) applications already mentioned. The second issue is the choice of frequencies for the top formation resistivity estimate. We will exploit the fact that when the frequency becomes sufficiently high, the apparent resistivity and the top formation resistivity should be of similar magnitude due to the skin-depth effect. The problem we have to address here is that high frequencies often are noisy. One reason is that transmitted current amplitudes usually are small for the higher frequencies. Another reason is the increased absorption with increased frequency that is typical for diffusive processes. There will always be a trade-off between the desire

for a higher frequency that make the apparent resistivity close to the top formation resistivity and a lower frequency that gives data that are sufficiently above the noise floor.

To summarize the results from Appendix B we form the impedance estimate,

$$Z_{xy}(\mathbf{x}_r, \omega|\mathbf{x}_s) = \frac{E_x(\mathbf{x}_r, \omega|\mathbf{x}_s)}{H_y(\mathbf{x}_r, \omega|\mathbf{x}_s)}, \tag{13}$$

resulting in the apparent resistivity estimate,

$$\rho_f(\mathbf{x}_r, \omega_l|\mathbf{x}_s) = \frac{|Z_{xy}(\mathbf{x}_r, \omega_l|\mathbf{x}_s)|^2}{\mu_0 \omega}. \tag{14}$$

We derive an approximation for the top formation resistivity in equation B-17:

$$\langle \rho_f(\mathbf{x}_r) \rangle = \frac{1}{N_s} \sum_{\omega_l} \sum_{\mathbf{x}_s = \mathbf{x}_a(\omega_l)}^{\mathbf{x}_b(\omega_l)} \rho_f(\mathbf{x}_r, \omega_l|\mathbf{x}_s), \tag{15}$$

where the sum over ω_l is a sum over a group of frequencies or a single frequency — all of which have the property that field amplitudes are above the noise level at sufficiently large offsets and that the fields at these frequencies are mostly sensitive to the resistivity contrast between the seawater and the top formation. The sum over $\mathbf{x}_s$ is a sum over source-receiver offsets that are sufficiently large to have a dominant airwave contribution in the downgoing field. These are the offsets in which the CSEM fields are most similar to MT fields. The normalization factor N_s equals the number of samples in the sum.

The upgoing field below the seabed can then be expressed:

$$E_x^U(\mathbf{x}_r, \omega|\mathbf{x}_s) = \frac{1}{2}(E_x(\mathbf{x}_r, \omega|\mathbf{x}_s) - Z_f(\mathbf{x}_r) H_y(\mathbf{x}_r, \omega|\mathbf{x}_s)), \tag{16}$$

with

$$Z_f(\mathbf{x}_r) = \sqrt{-i\mu_0 \omega \langle \rho_f(\mathbf{x}_r) \rangle}. \tag{17}$$

The lower range of ω_l can be estimated from synthetic tests, as will be discussed below.

The impedance can be calculated using standard MT data, which are always available in a CSEM survey, either due to the source not being active or being active but too far away to be measurable for a given receiver. This is proposed by Chen and Alumbaugh (2011) for the purpose of airwave mitigation by calculating an approximation to the scattered field. Their resulting expression for the scattered field, $E_x^{\mathrm{SCAT}} = E_x^{\mathrm{CSEM}} - Z_{xy}^{\mathrm{MT}} H_y^{\mathrm{CSEM}}$, appears similar to the upgoing field as given in equation 1, but it is different because they use the impedance Z_{xy}^{MT} and not the characteristic impedance of the top formation as required by equation 1. However, the characteristic impedance of the top formation can in principle be estimated as the high-frequency limit of Z_{xy}^{MT} by similar procedures to what we have outlined above. Our reason for using active source data (CSEM) and not passive data (MT) in our estimation scheme is that MT fields normally are weak at 1 HZ and above for the marine case. We will demonstrate below that we need data at 1 Hz or preferably above 1 Hz to estimate the top formation resistivity.

Comparing inversion results

The inversion results using total electric data must be compared with the results using the upgoing electric fields. We can compare data misfits and closeness to the true model for synthetic data tests. The true model is in principle unknown for real data cases, and the data misfit becomes the most important quality measure, even if comparison between the geometry of the conductivity model and the geometry from seismic data is possible when seismic data are available. We need a convergence measure that is as objective as possible. Our proposal is to take the final model from the inversion using total electric data and the final model from the inversion using upgoing electric fields and perform postinversion modeling of electric and magnetic fields. The resulting fields are then compared directly with the observed fields. It is essential to use a weighting function of the same kind as the one used in the inversion. If not, only small offsets will contribute to the misfit. The weight function must also reflect the effects of noise and uncertainty. The noise and uncertainty contributions can roughly be divided into two types. An additive contribution $\eta(\omega)$ that depends on the receiver noise level plus noise from the environment such as MT, swell noise, and receiver vibration noise. The receiver noise is due to sensor thermal noise and amplifier voltage noise. There is also a multiplicative contribution to the uncertainty, here controlled by the parameter α that scales with the amplitude of the transmitted field. This term is mostly due to source and receiver calibration uncertainty and navigation uncertainty. The magnitude of α is approximately 3% for marine CSEM equipment as of 2011.

The misfit we use for the electric data is

$$\epsilon_E = \frac{1}{N} \sum_{\mathbf{x}_r, \omega, \mathbf{x}_s} \frac{|\Delta E_x^m(\mathbf{x}_r, \omega|\mathbf{x}_s)|^2}{\alpha^2 |E_x^{\mathrm{Obs}}(\mathbf{x}_r, \omega|\mathbf{x}_s)|^2 + \eta_E^2(\omega)}, \tag{18}$$

where the numerator is the squared absolute value of the difference between the observed and predicted data from the final model, $\sigma^m(\mathbf{x})$. The denominator is the corresponding estimate of the uncertainty in the measurement. The normalization N is the number of data points. The corresponding misfit for the magnetic data is

$$\epsilon_H = \frac{1}{N} \sum_{\mathbf{x}_r, \omega, \mathbf{x}_s} \frac{|\Delta H_y^m(\mathbf{x}_r, \omega|\mathbf{x}_s)|^2}{\alpha^2 |H_y^{\mathrm{Obs}}(\mathbf{x}_r, \omega|\mathbf{x}_s)|^2 + \eta_H^2(\omega)}. \tag{19}$$

The total misfit is

$$\epsilon_T = \epsilon_E + \epsilon_H. \tag{20}$$

RESULTS

This section will have two parts. The first part discusses the estimation of the top-formation resistivities, which gives the characteristic impedance used for up-down decomposition. The second part discusses the use of the upgoing electric fields in inversion.

Estimation of upgoing fields

As described above, we can exploit the airwave contribution at large offsets to stabilize the top-formation resistivity estimate. The close proximity of the transmitter and the sea surface in shallow water gives observed data above the receiver noise level at large offsets. The recorded data can look very clean, even at source-receiver offsets

above 10 km. Much of this energy is related to the airwave contribution. MT noise does not affect the top-formation resistivity estimates — primarily because the MT field above 1 Hz generally is weak in the marine case, but note also that the MT signal can be approximated by a vertically propagating field just as the airwave. Thus, any MT contribution in the frequency band we use may help to stabilize the top-formation resistivity estimate. The derivation starting with equation B-9 assumes vertically propagating fields and does not depend on having an electric dipole transmitter as the source. The swell noise contribution can be expected to be small because it has its main contributions below 1 Hz.

The synthetic examples to follow are performed with a plane-layer full-waveform modeling scheme (Løseth and Ursin, 2007). The model used for the synthetic data tests is shown in Figure 1. For the examples given below, only parameters related to the water layer and the top formation are changed. The water layer is 50 m. The top-formation resistivity is 1 or 3 Ωm. The top-formation layer

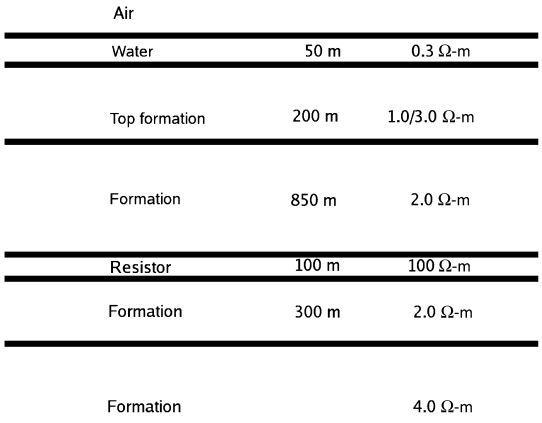

Figure 1. The model used in the synthetic data examples. The water depth is 50 m. The top-formation resistivity is either 1 or 3 Ωm. The remaining part of the model is constant for all examples.

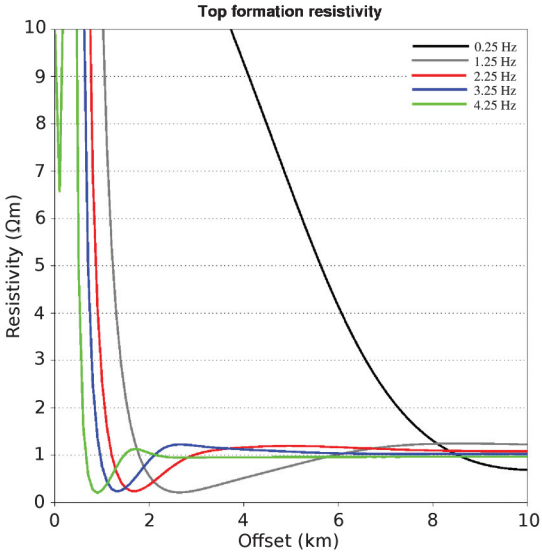

Figure 2. Top-formation resistivity estimates as a function of source-receiver offset. The water depth is 50 m, and the true top-formation resistivity is 1 Ωm.

is 200 m thick. The formation below the top formation has a resistivity of 2 Ωm. A top-formation layer of 3 Ωm is obviously more challenging with the proposed method because the relatively higher resistivity here increases sensitivity to deeper layers.

Synthetic data

The case with a water depth of 50 m and top-formation resistivity of 1 Ωm is shown in Figure 2. The curves are for the top-formation resistivity before averaging as given by equation 14. All curves are obviously in error at small source-receiver offsets. This is expected because the assumption of vertically propagating fields is poor in this offset interval. The proposed scheme is based on data from intermediate and large offsets in which the assumption of vertically propagating fields is acceptable. The 0.25 Hz estimate (black curve) of the top-formation resistivity is poor. The most likely reason is that the plane-wave approximation does not hold for the displayed offset range at this low frequency (Andréis et al., 2009). Anyway, data at these low frequencies are not of interest for our purpose because they are too sensitive to the deeper part of the formation due to the relatively large skin depth. The improvement in the top-formation resistivity function at 1.25 Hz (gray curve) is clear, but only at offsets above 7 km. The top-formation resistivity is slightly overestimated for this frequency; however, up-down decomposition is fairly robust with respect to the choice of top-formation resistivity. We will demonstrate this robustness in the real data examples that follow. The remaining (colored) curves are for frequencies above 2 Hz. All give good estimates of the top-formation resistivity and improve with increased frequency. The offsets in which the curves level off and become constant with respect to offset give a very good indication of the start of the offset interval where the data can be trusted for the top-formation resistivity estimate. We will use this property in the analysis of real data. We have also inspected the phase as a function of offset for the impedance given in equation 13. Vertically propagating fields are recognized by a close-to-flat phase curve as a function of offset and with a phase of approximately −45°. The correlation of this criterion with the criterion we use for the apparent resistivity is very good. We also note that the smallest offset for the applicable offset interval decreases with increasing frequency. This indicates a trade-off that must be handled for real data. High-frequency data can give accurate estimates even at relatively small offsets, but are potentially noisy for increasing offsets with a large standard deviation for estimates as given by equation 15. Slightly lower frequencies can give acceptable estimates with a smaller standard deviation.

The only change done for the simulation giving the data in Figure 3 is that the top-formation resistivity is increased from 1 to 3 Ωm. In this case, the 0.25 and 1.25 Hz data are useless for top-formation resistivity estimated. However, the estimates for frequencies above 2 Hz can be used. All these curves show an underestimation of the top-formation resistivity because the high top-formation resistivity used in the simulation increases the sensitivity in the data to the underlying formation, which has a resistivity of 2 Ωm. The 2.25 and 3.25 Hz data give an average estimate of approximately 2.75 Ωm instead of the correct value of 3 Ωm. The 4.25 Hz data give an average estimate of 2.85 Ωm. All of these estimates give sufficiently good results when used for up-down decomposition.

The examples given here represent a subset of the results from a larger set of simulations that we have carried out. Analysis of these simulations gives some rules of thumb with regard to the choice of

ω_l or the corresponding frequency f_l and usable offset ranges. First, if the resistivity in the top formation is smaller than the deeper formation, then frequencies down to 2 Hz can be used in the top-formation resistivity estimates. The effective offset range can be expected to be reduced when the water depth increases because larger source-receiver separations are required for the plane-wave assumption to be valid. On the other hand, the need for up-down decomposition is also reduced with increased water depth. Second, if the resistivity in the top formation is larger than the deeper formation, then frequencies down to 2 Hz can be used in the top-formation resistivity estimates in very shallow water, but higher frequencies are required as the water depth increases. Again, the effective offset range can be expected to be reduced for increasing water depth because the smallest usable source-receiver distance, above where the vertically propagating field assumption is valid, increases. The results from the synthetic tests indicate that we can obtain fairly reliable top-formation resistivity estimates if there are no substantial resistivity contrasts from the seabed and down to half a skin depth below the seabed. Thus, if the first 500 m of the top formation is relatively homogeneous, then data at 1 Hz can be used for the estimates even if the top-formation resistivity is 4 Ωm. This is the situation also when the water depth is 250–350 m. The usable offset range is then from 8 to 10 km and above.

Real data

The first real case is for electromagnetic data acquired in a water depth of 60 m. The conductivity of the seawater was logged to 5.35 S/m. The source waveform was a broadband square wave (Mittet and Schaug-Pettersen, 2008) with a first harmonic of 0.33 Hz. High currents were transmitted on the first four harmonics, [0.33, 0.67, 1.0, 1.33 Hz] with the corresponding current amplitudes [1038, 900, 437, 737 A]. Of these, only the first and fourth harmonics are shown in Figure 4. These are shown for comparison and are not used in the estimate of the top-formation resistivity. Some of the higher harmonics had reasonably high current amplitudes [2.33, 3.33, 4.0 Hz] with [181, 178, 116 A]. The 3.33 and 4.0 Hz data were used in combination for the estimate of the top-formation resistivity. The offset range from 4 to 9.5 km was used for both frequencies. Estimation by equation 15 gave an average top-formation resistivity for this receiver $\langle \rho_f(\mathbf{x}_r) \rangle$ equal to 1.62 Ωm with a standard deviation $\Delta\rho_f(\mathbf{x}_r)$ of 0.28 Ωm. The standard deviation is in this case 17% of the average value.

These values are then used in up-down decomposition. The results for the amplitudes are shown in Figure 5 and for the phases in Figure 6. The data in Figures 5 and 6 are for the first harmonic at 0.33 Hz. To have an indication of the robustness of the up-down decomposition, four characteristic impedances are used. The characteristic impedance of seawater is Z_w, where the measured conductivity/resistivity is used, and Z_f is given by equation 17. Further on

$$Z_-(\mathbf{x}_r) = \sqrt{-i\mu_0\omega[\langle \rho_f(\mathbf{x}_r)\rangle - \Delta\rho_f(\mathbf{x}_r)]},$$
$$Z_+(\mathbf{x}_r) = \sqrt{-i\mu_0\omega[\langle \rho_f(\mathbf{x}_r)\rangle + \Delta\rho_f(\mathbf{x}_r)]}, \qquad (21)$$

where $\Delta\rho_f(\mathbf{x}_r)$ is the standard deviation of the top-formation resistivity estimate. The up-down decomposition is performed for the characteristic impedance based on the average value of the top-formation resistivity, but also for characteristic impedances Z_- and Z_+ given by resistivities that are one standard deviation below and one standard deviation above the average. This is done to evaluate the robustness of the up-down decomposition procedure. The black curve in Figure 5 is the observed inline electric field without up-down decomposition. The gray curve is the upgoing electric field extracted using the characteristic impedance for seawater. The amplitude as a function of offset becomes nearly constant for large offsets just as for the observed data. This is a clear indication that a significant airwave component is still present in the upgoing field as can be expected from equation B-3. The green curve is the upgoing electric field extracted with the characteristic impedance based on the best estimate for the top-formation resistivity. The red and blue curves are upgoing electric fields using Z_- and Z_+, respectively.

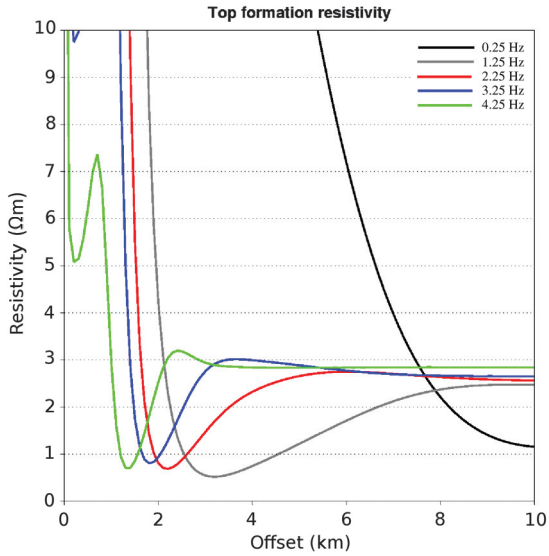

Figure 3. Top-formation resistivity estimates as a function of source-receiver offset. The water depth is 50 m, and the true top-formation resistivity is 3 Ωm.

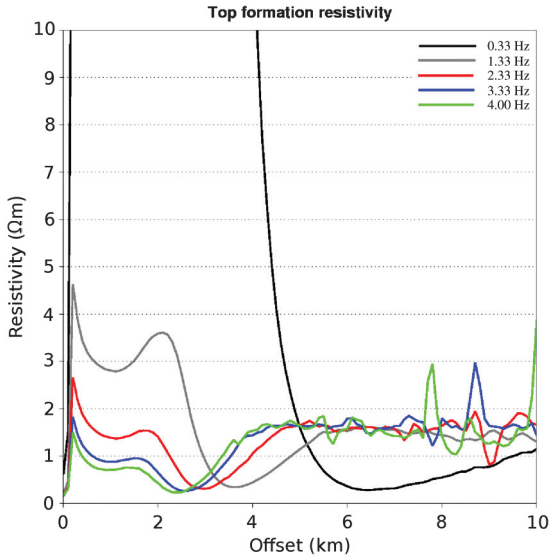

Figure 4. Top-formation resistivity estimates as a function of source-receiver offset. The water depth is 60 m.

Let us assume that either Z_- or Z_+ were used in the inversion of upgoing electric fields instead of Z_f. The standard deviation for the top-formation resistivity estimate is 17%. Thus, the amplitude of Z_+ is 8% larger than the amplitude of Z_f and the amplitude of Z_- is 8% smaller than the amplitude of Z_f. For the inversion kernel, this would imply that we do a reweighting of the magnetic contribution compared to the electric contribution that is $\pm 12\%$. The difference between 8% and 12% comes from a proper analysis of the phase terms. In Figure 5 we see a clear difference between doing up-down decomposition above or below the seabed. The curves for Z_f, Z_-, and Z_+ show the same qualitative behavior even if there are some amplitude differences at large offsets. The distinct flattening of the

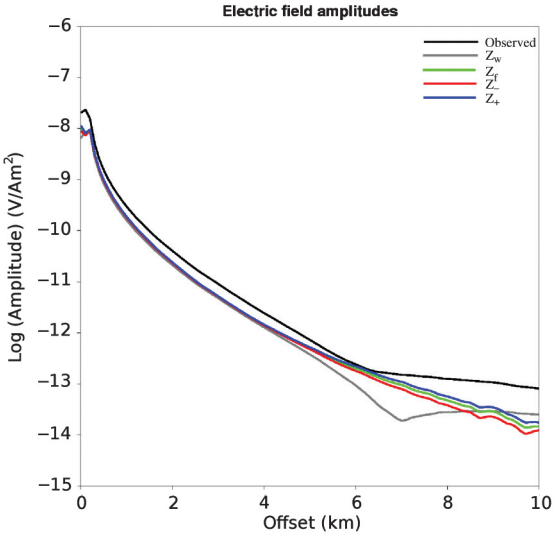

Figure 5. Amplitudes before and after up-down decomposition. The water depth is 60 m. The 3.33 and 4.0 Hz data were used in combination for the estimate of the top-formation resistivity. The plotted data are for the first harmonic at 0.33 Hz.

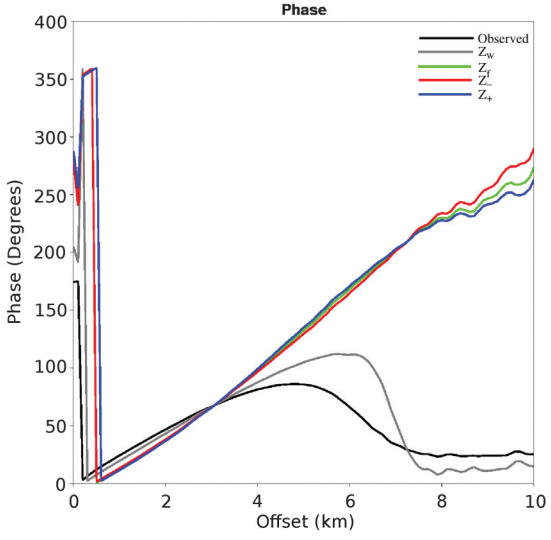

Figure 6. Phases before and after up-down decomposition. The water depth is 60 m. The 3.33 and 4.0 Hz data were used in combination for the estimate of the top-formation resistivity. The plotted data are for the first harmonic at 0.33 Hz.

amplitude curves at a large offset, which is characteristic for the observed field and the field that is decomposed above the seabed, is gone. The amplitude differences at a large offset that are of the order of $\pm 25\%$ could have had consequences if the exact upgoing field was required; however, for our formulation of inversion with upgoing electric fields, this is of much less concern because we apply the same characteristic impedance for up-down decomposition to observed and predicted data. We say that for the purpose of inversion of upgoing electric fields as formulated here, the amplitude results in Figure 5 indicate that up-down decomposition is a robust process. However, the phase curves can give an even stronger indication of the failure or success of airwave separation because the airwave contributions are easily identified by a high phase velocity.

The phase curves are given in Figure 6. A large airwave component is present in the observed field. This is evident from the roll-over behavior and the nearly constant phase as a function of offset at large offsets. It is also clear from the gray curve that Z_w does a poor job with regard to removing the airwave contribution. There is a large airwave component in this field evident from the roll-over behavior and nearly constant phase at large offsets. The behavior is similar to the observed field. In particular, a small gradient for the phase as a function of offset is indicative of a large phase velocity. A rough approximation to the phase ϕ as a function of offset, $x = |x_r - x_s|$, is

$$\phi(x) = \frac{\omega}{c} x, \tag{22}$$

where c is the effective phase velocity. A large phase velocity gives a small gradient because the gradient of the curve in equation 22 is inversely proportional to the phase velocity. The phase curves for Z_f, Z_-, and Z_+ are very different compared with those for the observed data or Z_w decomposed data; the steep gradient indicates a much lower phase velocity for these fields than for those sensitive to propagation in the air layer. The airwave contribution is strongly reduced for the Z_f, Z_-, and Z_+ decomposed data, and all choices will work fine if the up-down decomposition is used in combination with inversion.

The second real case is for electromagnetic data acquired in a water depth of 250 m. The conductivity of the seawater logged during acquisition was 3.35 S/m. The source waveform was also here a broadband square wave. The first harmonic was 1.0 Hz. It was known prior to the survey that the subsurface, including the top formation, was relatively resistive. This is the reason for the high first harmonic of the transmitted waveform. High currents were transmitted on the first four harmonics [1.0, 2.0, 3.0, 4.0 Hz] with corresponding current amplitudes [663, 747, 337, 550 A]. There was also a fairly high current transmitted at 10.0 Hz, namely, 378 A. It turned out that the 3.0 and the 10.0 Hz data were too noisy for top-formation resistivity estimation. The curves in Figure 7 are for 1.0, 2.0, and 4.0 Hz. The 1.0 Hz curve is there for comparison. Only the 2.0 Hz curve and the 4.0 Hz curve have potential for top-formation resistivity estimation. Both curves show indication of a constant resistivity function as a function of offset for large offsets. This is the property we seek because this property defines the useful offset interval. However, it is clear that the 4.0 Hz curve is much more noisy than the 2.0 Hz curve. The 2.0 Hz data were used for top-formation resistivity estimation. The offset range from 6.5 to 10 km was used. This resulted in an average top-formation resistivity estimate of 2.8 Ωm with a standard deviation of 0.4 Ωm. The

standard deviation is 14% of the average value. The 4.0 Hz data give a similar top-formation resistivity estimate, but the standard deviation becomes 50% of the average value. The data in Figures 8 and 9 are for the first harmonic at 1.0 Hz. The amplitude curves in Figure 8 can be compared with the amplitude curves in Figure 5, and the phase curves in Figure 9 can be compared with the corresponding curves in Figure 6. The general behavior is similar to what we observe for the 60-m-water-depth data set. We have strong indications that a large part of the airwave can be suppressed even if there is some uncertainty in the top-formation resistivity estimate.

Inversion of total fields and decomposed upgoing fields

We now have at hand a method to estimate the top-formation resistivity required to do up-down decomposition below the seabed. We intend to use the resulting upgoing electric fields as misfit kernels for the inversion. This is mainly a shallow-water technique in which the idea is to reduce the contribution of the airwave at intermediate and large offsets. A beneficial side effect of extracting the upgoing electric field is that contributions in the observed data from any downgoing MT fields are strongly suppressed. The first question that must be answered is if this scheme gives improvements compared to the standard procedure. Part of the answer can be found by performing tests on synthetic data, but before we do that we need to consider the influence of regularization. The amplitudes for the kernel of the data-space misfit functional will be different when we compare inversion of total electric data with inversion of upgoing electric data. If we look back at Figure 5, we observe that the amplitudes of the total field are larger than the upgoing field. This is an indication of constructive interference between the upgoing and downgoing fields. However, if we inspect Figure 8 we observe that the total field is smaller than the upgoing field for offsets up to 7 km; hence, there is destructive interference between the upgoing and downgoing fields.

It is straightforward to verify that the data-space part of the misfit ε^D as a function of the iteration number will differ depending on what kind of inversion kernel is used. Hence, the effect of the model-space regularization may vary with the type of data-space kernel used. We have performed multiple inversion runs for synthetic and real data in which the value of the Tikhonov parameter in equation 12 is varied. We have compared final results in which the ratio of the model-space error to the data-space error is identical for inversion of total electric field data and upgoing electric field data. We have also compared final results in which the model-space error is identical for inversion of total electric field data and upgoing electric field data. We have further varied the Tikhonov parameter systematically over a range of values in the neighborhood of our preferred value to investigate the robustness with respect to the choice of this parameter. We find that our results are not very

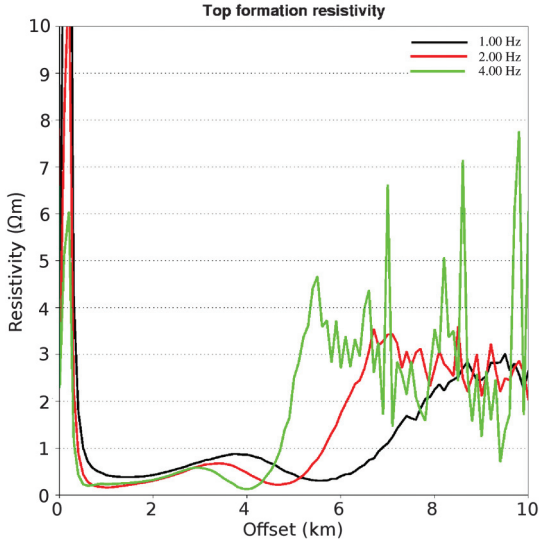

Figure 7. Top-formation resistivity estimates as a function of source-receiver offset. The water depth is 250 m.

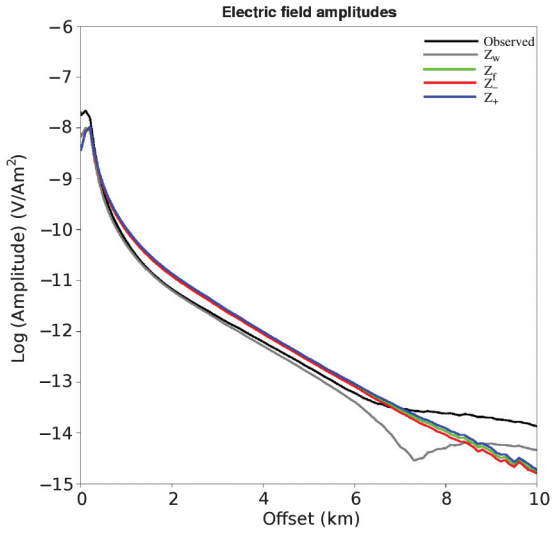

Figure 8. Amplitudes before and after up-down decomposition. The water depth is 250 m. The top-formation resistivity estimate is based on the 2 Hz data. The plotted data are for the first harmonic at 1.0 Hz.

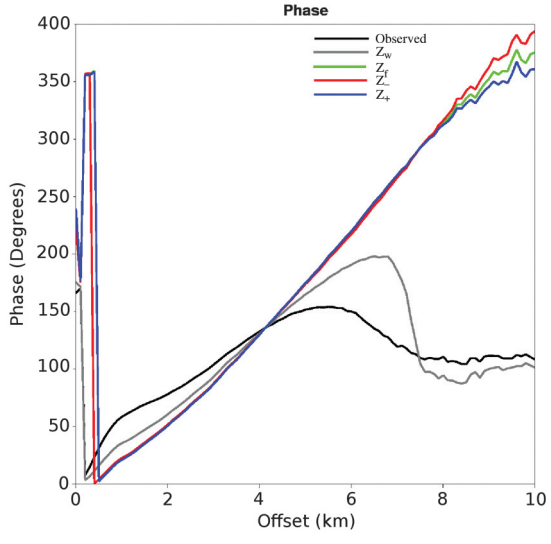

Figure 9. Phases before and after up-down decomposition. The water depth is 250 m. The top-formation resistivity estimate is based on the 2 Hz data. The plotted data are for the first harmonic at 1.0 Hz.

sensitive to the choice of the model-space regularization contribution. Increasing the Tikhonov parameter yields, as expected, increased horizontal smearing of the final resistivity model, but it does not change the total misfit significantly. For the results, we display in the following: we have chosen to tune the Tikhonov parameter such that the ratio of the model-space error to the data-space error is identical for inversion of total electric field data and upgoing electric field data at the final iteration.

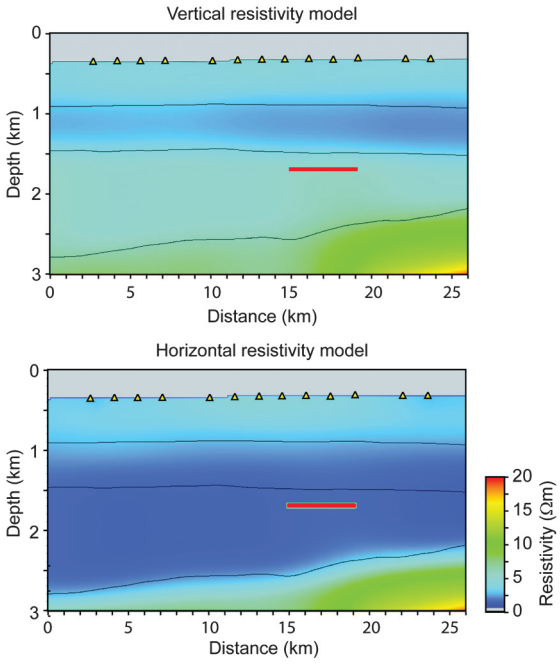

Figure 10. True model for inversion test on synthetic data.

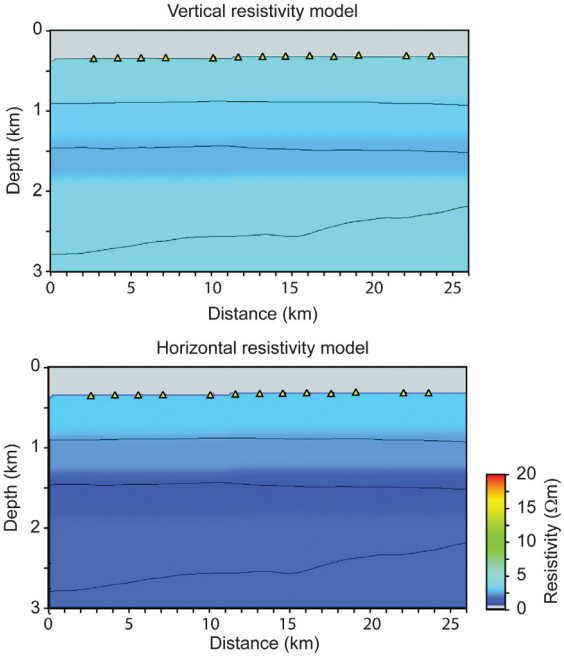

Figure 11. Start model for inversion test on synthetic and real data.

Synthetic data

The true model used for the synthetic data tests is shown in Figure 10. This model is inspired by the real data case we discuss in the next section. The background resistivity is laterally varying within defined strata. The maximum resistivity is 30 Ωm in the deepest part of the model. A 50-Ωm resistor, 4500 m long and 50 m thick, is located 1350 m below the seabed. The water depth varies between 320 and 350 m. The top-formation vertical resistivity is 3.9 Ωm, and the top-formation horizontal resistivity is 3.5 Ωm. The four frequencies used were 0.25, 0.5, 0.75, and 1.0 Hz. The current amplitudes were 950, 896, 431, and 683 A, respectively. The 1.0 Hz data were used for top-formation resistivity estimates. This low frequency can be used in this case because the resistivity is relatively homogeneous in the first 500 m below the seabed. The estimated top-formation resistivities were within 5% of the true value for the top-formation horizontal resistivity. The estimated values ranged from 3.35 to 3.45 Ωm along the receiver line.

The initial model for the inversion is shown in Figure 11. We will use this initial model for our synthetic and real data examples. The initial model consists of a few layers with resistivity values ranging from 1.0 to 3.6 Ωm. This initial model was estimated from the real data using a plane layer TIV inversion scheme. A small subset of the receivers was used. Each of these receivers had in common that the difference between data on the intowing side and the data on the outtowing side was very small. This is an indication of modest lateral resistivity variations locally, and the plane layer assumption can be assumed to be reasonably good. The 1D resistivity models were averaged. The resulting 1D model was used from the seabed and down to 3 km for the entire 2D model. The top-formation vertical resistivity is 3.6 Ωm, and the top-formation horizontal resistivity is 2.8 Ωm. These values differ from those of the true model. The synthetic and real inversion examples shown here were also started with a half-space below the seabed as initial model. The results was very similar to what we present here. This indicates that the Gauss-Newton scheme is fairly robust with respect to the choice of initial model.

The result of using the total electric fields for the kernel of the misfit functional is shown in Figure 12. The resistor is placed at the correct depth, but the resolution is low compared to the true model. The recovered peak resistivity of the target is 13 Ωm. The lateral extent of the recovered resistor is underestimated by 1.5–2 km. The background horizontal and vertical resistivities are reasonably well recovered down to a 3000-m depth. The resistor is not recovered in the horizontal resistivity model. The effect is well known and is due to the fact that the horizontal electric and magnetic fields are insensitive to thin resistive layers.

The result of using the upgoing electric fields is shown in Figure 13. The resistor is placed at the correct depth, and the resolution is improved compared to the previous case. The recovered peak resistivity of the target is 32 Ωm. This is fairly close to the true value and an improvement compared with using total electric field data only for the optimization. The transverse resistance of the anomalies are very close for the models in Figures 12 and 13. The value is approximately 3000 Ωm^2 in both cases, this is in fact an overestimate compared to the true value of 2500 Ωm^2. The deviation is within expected bounds. A sensitivity study of this effect is performed in Mittet et al. (2008). Using the results from Figure 13 of that paper, we note that for a true transverse resistance

of 2500 Ωm^2, the total error can be at a minimum for models with transverse resistances in the range 1900 to 3100 Ωm^2.

The lateral extent of the recovered resistor in Figure 13 is very close to the true value, again an improvement over using total electric field data only. The background horizontal and vertical resistivities are nicely recovered. In addition, there seems to be a slight improvement in the shallow part of the horizontal resistivity when comparing with the standard scheme and an increase in sensitivity at depth for the vertical resistivity. Again we observe that the resistor is not recovered in the horizontal resistivity model due to the insensitivity of the horizontal electric fields to thin resistive layers.

The top-formation vertical and horizontal resistivities are 3.8 and 3.7 Ωm, respectively, for the model in Figure 12 and 3.8 and 3.4 Ωm, respectively, for the model in Figure 13. The true values are 3.9 and 3.5 Ωm. The resistivities in the upper part of the formation are best determined by using the upgoing electric field as the kernel for the misfit function.

Our next step is to take the model shown in Figure 12 and perform a postinversion modeling of electric and magnetic data. The values of the α and $\eta(\omega)$ parameters of equations 18 and 19 determine the data uncertainty. The value of α is, in principle, frequency and offset dependent. A thorough error propagation analysis shows that the offset dependence is weak at intermediate and large offsets. The same analysis also shows that the frequency dependence is weak. Here we use an average value of $\alpha = 0.03$. The additive noise is frequency dependent. We have collected noise data from surveys performed at various water depths and at different latitudes. The general trend is that the additive noise increases as the water depth is reduced. This is reasonable because we have a higher contribution from MT signals with reduced water depth. Also swell noise becomes an issue in shallow water. The additive noise also does increase with high latitudes. This is again an effect of increased MT signals. We have chosen some typical shallow water values for the additive noise:

$$\begin{aligned}
\eta_E(0.25\ \text{Hz}) &= 9\times10^{-10}\ \text{V/m}, \\
\eta_E(0.50\ \text{Hz}) &= 6\times10^{-10}\ \text{V/m}, \\
\eta_E(0.75\ \text{Hz}) &= 3\times10^{-10}\ \text{V/m}, \\
\eta_E(1.00\ \text{Hz}) &= 3\times10^{-10}\ \text{V/m},
\end{aligned} \tag{23}$$

for the electric data and

$$\begin{aligned}
\eta_H(0.25\ \text{Hz}) &= 9\times10^{-7}\ \text{A/m}, \\
\eta_H(0.50\ \text{Hz}) &= 3\times10^{-7}\ \text{A/m}, \\
\eta_H(0.75\ \text{Hz}) &= 2\times10^{-7}\ \text{A/m}, \\
\eta_H(1.00\ \text{Hz}) &= 2\times10^{-7}\ \text{A/m},
\end{aligned} \tag{24}$$

for the magnetic data.

Equation 18 gives $\epsilon_E = 5.7\times10^{-3}$, and equation 19 gives $\epsilon_H = 8.2\times10^{-3}$. The magnetic data did not contribute to the inversion in this case. Still, the error from the magnetic contribution is fairly small. The total error is $\epsilon_T = 1.39\times10^{-2}$.

We repeat the procedure for the model shown in Figure 13 and obtain $\epsilon_E = 6.0\times10^{-3}$, $\epsilon_H = 7.3\times10^{-3}$, and $\epsilon_T = 1.33\times10^{-2}$. The magnetic data did contribute to the inversion in this case, and it is reasonable to find that the misfit due to the contribution from magnetic data is slightly reduced; however, there is a small increase in the contribution from the electric data. The improvement in the total error is approximately 5% when the upgoing electric fields are used in the misfit kernel. The improvement in data fit seems small, but the 5% reduction of the total error gives a resistivity model that is much closer to the true model.

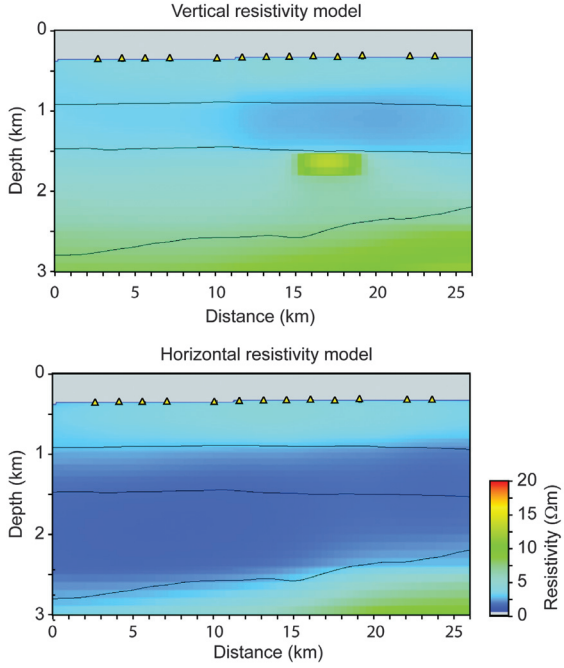

Figure 12. Final model for the inversion test on synthetic data. Total electric field inversion kernel.

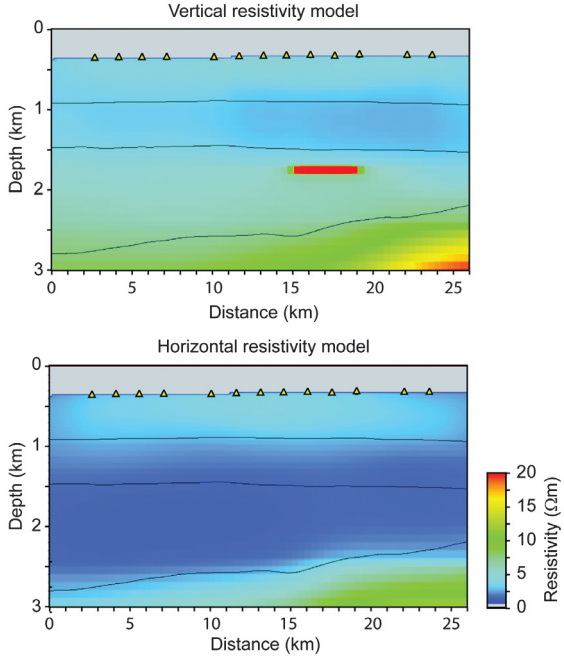

Figure 13. Final model for the inversion test on synthetic data. Upgoing electric field inversion kernel.

Real data

We need an estimate of the top-formation resistivities for the real data inversion example. These values are used for the extraction of the upgoing fields. The estimation curves for one of the receivers are shown in Figure 14. In this case we used the 1-Hz data from 9 to 13 km for the estimation. The result was a top-formation resistivity of 3.3 Ωm with a standard deviation of 0.25 Ωm. All receivers gave similar results. We would have preferred to use data above 1 Hz for the top-formation resistivity estimates, but the transmitted current amplitudes above 1 Hz were too small to give reliable estimates for this data set. From synthetic tests, we know that 1 Hz can be used for these types of estimates if the upper 500 m of the formation are relatively homogeneous, and we believe this to be the case here.

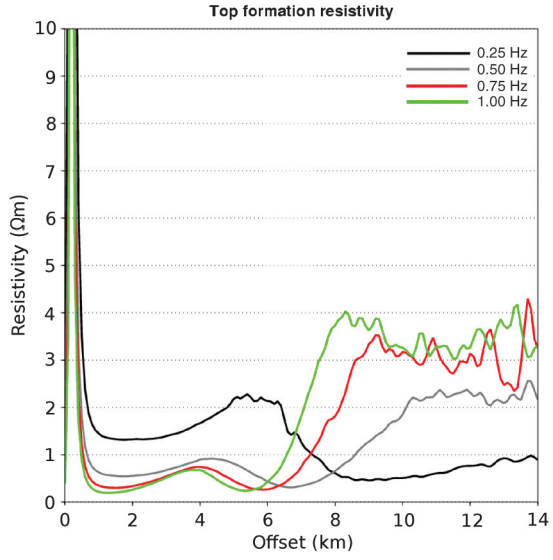

Figure 14. Top-formation resistivity estimates as a function of source-receiver offset. The frequency used for top-formation resistivity estimation is 1.0 Hz. The water depth is 330 m.

The initial model is the same as for the synthetic test and is shown in Figure 11. Figure 15 shows the recovered resistivity models by the standard procedure in which only the electric fields are used in the misfit kernel. A resistive object is recovered at distances of 15 to 21 km and at a depth of 1600 m. The peak resistivity recovered for the resistor is 33.5 Ωm.

The result of using the upgoing electric fields in the misfit kernel is shown in Figure 16. The resistive object is thinner compared with the result from the standard inversion. The lateral dimension is increased with 2 km compared with the case shown in Figure 15. The same effects are observed in the synthetic data test. The peak resistivity is 86.5 Ωm. The recovered transverse resistances of the anomalies for the models in Figures 15 and 16 are comparable and have a value of 5500 Ωm^2.

The background resistivity is similar for the two real data cases down to 2400 m. From this depth and below the misfit kernel based on the upgoing electric fields result in a model with higher resistivity. A similar effect is observed for the synthetic data example. There is a reduction in the vertical resistivity below the resistor in the deeper part of the models shown in Figures 15 and 16. The effect may be real but can also be a shadow effect because this part of the model is located below the thin resistive layer.

Again we perform postinversion modeling for the final models and compare the predicted data with the observed data. For the standard procedure, we find that equation 18 gives $\epsilon_E = 6.6 \times 10^{-3}$ and equation 19 gives $\epsilon_H = 1.12 \times 10^{-2}$ with a total misfit $\epsilon_T = 1.78 \times 10^{-2}$. When upgoing electric fields are used in the kernel of the misfit function, we find $\epsilon_E = 8.8 \times 10^{-3}$,

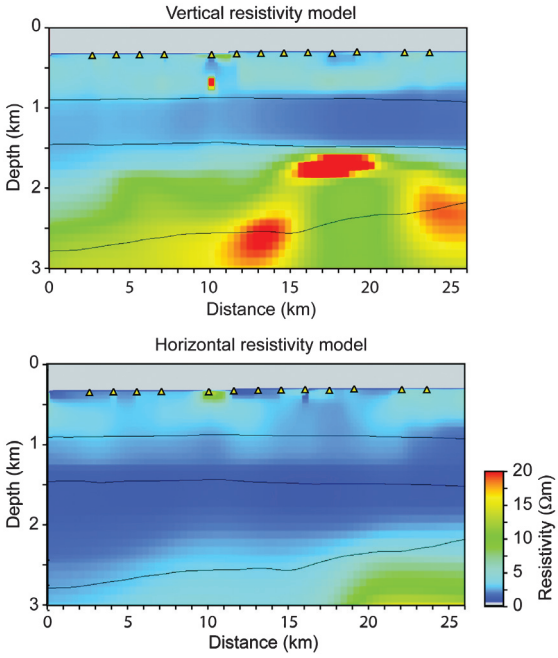

Figure 15. Final model for the inversion test on real data. Total electric field inversion kernel.

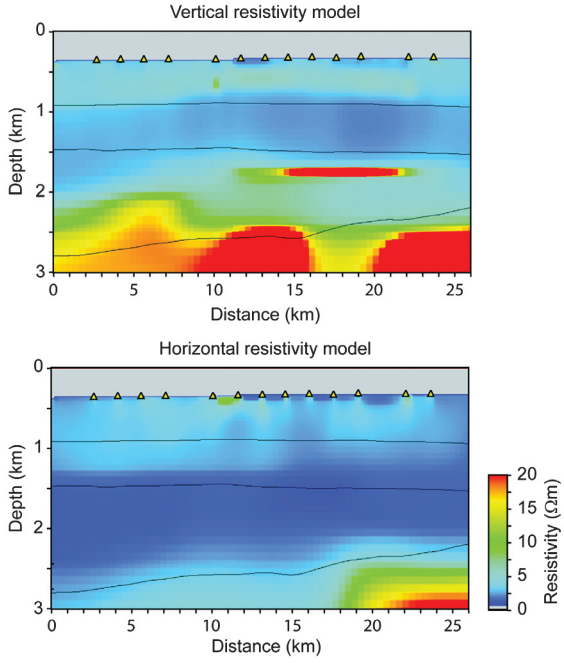

Figure 16. Final model for the inversion test on real data. Upgoing electric field inversion kernel.

$\epsilon_H = 6.9 \times 10^{-3}$, and $\epsilon_T = 1.57 \times 10^{-2}$. The total error is reduced by 13%. As for the synthetic case, we observe that the contribution from the electric fields increases slightly whereas the contribution from the magnetic fields is reduced.

The above example is for the case in which the ratio of the regularization error to the data error for total electric fields kernels $\varepsilon_T^M/\varepsilon_T^D$ equals the ratio of the regularization error to the data error for upgoing electric field data kernels, $\varepsilon_U^M/\varepsilon_U^D$. We have investigated the effect of regularization by varying the Tikhonov parameter for the inversion of the total electric fields. The purpose is to see if we can reduce the total data-space error and improve on the image in Figure 15. Let us denote the Tikhonov parameter that gives the above results λ_1. If we change the Tikhonov parameter as $\lambda_2 = 2 \times \lambda_1$, we get a situation in which $\varepsilon_T^M = \varepsilon_U^M$. The error contributions from the electric fields and magnetic fields are then $\epsilon_E = 6.3 \times 10^{-3}$ and $\epsilon_H = 1.13 \times 10^{-2}$ with a total misfit of $\epsilon_T = 1.76 \times 10^{-2}$. The total misfit for the total electric field data kernel is reduced by 1% by increasing the effect of regularization with a factor of two. If we use a Tikhonov parameter $\lambda_3 = 5 \times \lambda_1$, we have $\varepsilon_T^D + \varepsilon_T^M = \varepsilon_U^D + \varepsilon_U^M$ at the final iteration. In this case we find $\epsilon_E = 6.5 \times 10^{-3}$ and $\epsilon_H = 1.13 \times 10^{-2}$ with a total misfit of $\epsilon_T = 1.78 \times 10^{-2}$. This is the same total misfit as for the case displayed in Figure 15. We find the smallest total misfit for the total electric field data kernel by using $\lambda_4 = 3 \times \lambda_1$. The electric and magnetic error contributions are $\epsilon_E = 6.3 \times 10^{-3}$ and $\epsilon_H = 1.10 \times 10^{-2}$ with a total misfit of $\epsilon_T = 1.73 \times 10^{-2}$. This is a reduction of 3% compared to the base case; however, the total misfit is still 10% above the results obtained by inverting upgoing electric fields. The general trend we observe by increasing the Tikhonov parameter and hence the strength of the regularization is that the thin resistor is sharpened in the depth direction, but it is always more blurred than the results obtained by inverting upgoing electric fields. The lateral extent is not changed.

The observed electric and magnetic fields and the predicted fields from postinversion modeling are shown in Figure 17. The observed data are given by the black curves. The green curves are predicted data from the final model obtained by using the upgoing electric fields in the misfit kernel. The blue curves are predicted data from the final model obtained by using the total electric fields in the misfit kernel. The frequency is 1.0 Hz. This was the highest frequency used for the inversions and also was the frequency used for the estimation of the top-formation resistivity. The data fit is better for 0.25, 0.5, and 0.75 Hz data than for the displayed 1.0 Hz data. The curves in Figure 17 reflect what we observe for the total error. The fit between observed and predicted magnetic data is slightly better when the upgoing electric fields are used as the misfit kernel compared with the total electric field. The fit between the observed and the predicted electric data is slightly worse when the upgoing electric fields are used as the misfit kernel compared with the total electric field. However, when calculating the total misfit, we find that this is more than compensated for by the improved fit for the magnetic data. In particular we observe a better fit for the magnetic phase data at large offsets. A close inspection of the amplitude curves show the same behavior, but for high offsets the fit is improved also for the electric data using the upgoing-field inversion kernel.

A final step for our scheme is to estimate the top formation resistivity from the predicted data. This is a consistency check. Using the predicted data from the final model obtained by using the upgoing electric fields in the misfit kernel, we find the same top-formation resistivity as the estimate based on the observed data. This follows as a consequence of the small difference between the observed electric and magnetic fields and the predicted electric and magnetic fields in this case.

The top-formation resistivity is underestimated by 12% if we use predicted data from the model based on inversion of the total field. The reason is that for the large offsets used for top-formation

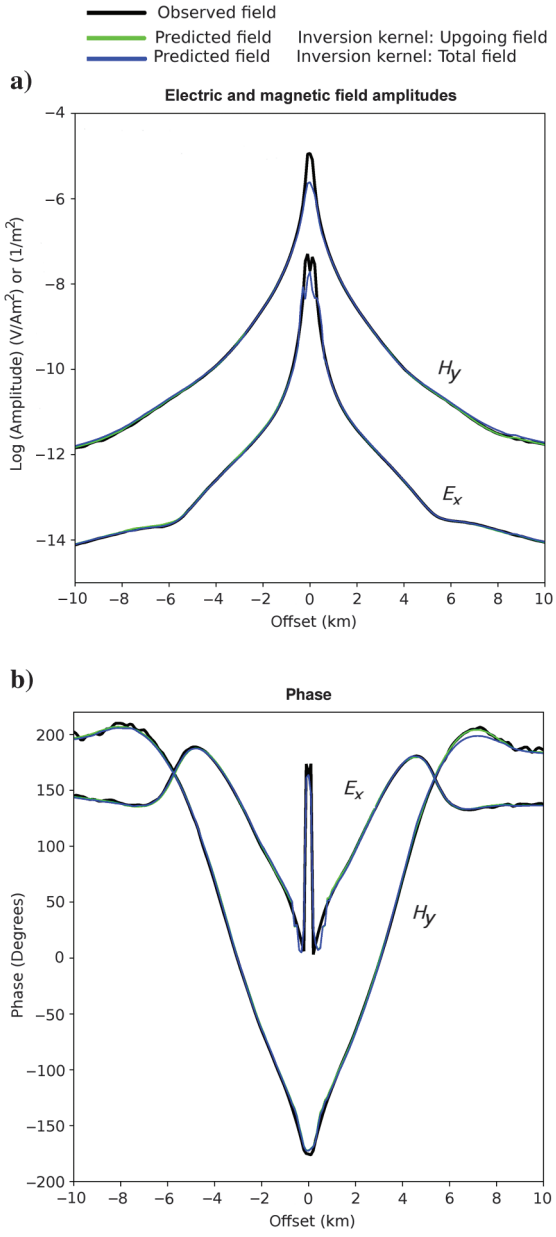

Figure 17. Observed and predicted electric and magnetic data: (a) amplitude curves and (b) phase curves. The frequency is 1.0 Hz. Black curves are the observed fields. Green curves are the postinversion predicted data using the final model obtained from inversion with the upgoing electric field as misfit kernel. Blue curves are the postinversion predicted data using the final model obtained from inversion with the total electric field as misfit kernel.

resistivity estimates, the amplitude of the electric field is overestimated by 3% and the amplitude of the magnetic field is overestimated by 9.5%. The net effect is a 12% underestimation of the apparent resistivity, which is in accordance with equations 13 and 14.

The top-formation resistivity resulting from the inversion shows some receiver footprint effects in Figures 15 and 16. Neglecting those, we estimate the average top-formation vertical resistivity in Figure 16 to be 4.4 Ωm. The corresponding average horizontal top-formation resistivity is 3.2 Ωm, which is in good agreement with our initial estimate of 3.3 Ωm. Similar values for the models in Figure 15 are 4.2 Ωm for the top-formation vertical resistivity and 3.1 Ωm for top-formation horizontal resistivity.

CONCLUSIONS

We have proposed a data-driven method to estimate the resistivity immediately below the seabed at a given receiver location. The purpose is to use this top-formation resistivity estimate for up-down decomposition of the electromagnetic data. The resulting upgoing field is then used as the misfit kernel in an inversion scheme. This strategy is targeted for data acquired in shallow water.

The resistivity of the top formation can in most cases be estimated from the recorded CSEM data with sufficient accuracy to perform the decomposition of the electromagnetic field in upgoing and downgoing constituents below the seabed. The up-down decomposition procedure is robust and tolerates uncertainties in the top-formation resistivity estimates of at least 15%.

Inversion using the upgoing electric field as the kernel in the misfit functional leads to an implicit inclusion of magnetic data in the processing. We find that the resolution improves when magnetic data are included in the inversion scheme, in terms of target and background resistivity. Inversion based on upgoing electric fields is a robust method because it is only the relative weight between electric and magnetic data misfits that changes with the top-formation characteristic impedance estimate. The postinversion modeling tests show that the sum of weighted electric and magnetic errors is reduced when magnetic data are included in the inversion scheme.

ACKNOWLEDGMENTS

We thank EMGS ASA for permission to publish this work. We also thank Kristian Rymann Hansen for his contributions to the development of our 2.5D inversion scheme. We thank Lars Løseth, Anandaroop Ray, and two anonymous reviewers for their constructive comments.

APPENDIX A

DECOMPOSITION OF ELECTROMAGNETIC FIELDS INTO UPGOING AND DOWNGOING VERTICAL COMPONENTS FOR TIV MEDIA

The 2.5D inversion scheme used here is TIV, which implies that the horizontal and vertical resistivity/conductivity are estimated. For the estimation of the top-formation resistivity, we only need to estimate the horizontal resistivity. This is the case if the electromagnetic field is well approximated by a vertically propagating field. The explanation below follows Amundsen et al. (2006) and Løseth and Ursin (2007) closely.

The Fourier transforms between horizontal space and wavenumber coordinates and time and frequency for a function F are

$$F(k_x,k_y,\omega)=\int_{-\infty}^{\infty}\int_{-\infty}^{\infty}\int_{-\infty}^{\infty}dxdydtF(x,y,t)e^{-i(k_xx+k_yy-\omega t)},$$
$$F(x,y,t)=\frac{1}{(2\pi)^3}\int_{-\infty}^{\infty}\int_{-\infty}^{\infty}\int_{-\infty}^{\infty}dk_xdk_yd\omega F(k_x,k_y,\omega)e^{i(k_xx+k_yy-\omega t)}, \tag{A-1}$$

where k_x and k_y are wavenumbers and ω is angular frequency. The horizontal slownesses are

$$p_i=\frac{k_i}{\omega}, \tag{A-2}$$

with $p^2=p_x^2+p_y^2$.

The Maxwell equations in a source-free region for a TIV medium are

$$\nabla\times\mathbf{E}=-\mu_0\partial_t\mathbf{H},$$
$$\nabla\times\mathbf{H}=(\boldsymbol{\sigma}+\boldsymbol{\varepsilon}\partial_t)\mathbf{E}, \tag{A-3}$$

where $\boldsymbol{\sigma}$ and $\boldsymbol{\varepsilon}$ are 3×3 tensors with only diagonal elements different from zero.

The Maxwell equations are transformed to the horizontal wavenumber and frequency and the E_z and H_z components are eliminated algebraically to give

$$\partial_z\mathbf{b}=i\omega\mathbf{A}\mathbf{b}, \tag{A-4}$$

where $\mathbf{b}=[E_x,E_y,-H_y,H_x]^T$ and the 4×4 system matrix $\mathbf{A}$ can be partitioned into four 2×2 submatrices,

$$\mathbf{A}=\begin{bmatrix}\mathbf{0} & \mathbf{A}_1\\ \mathbf{A}_2 & \mathbf{0}\end{bmatrix}, \tag{A-5}$$

where the diagonal ones are zero.

The complex permittivity tensor containing the horizontal and vertical permittivities and conductivities is

$$\tilde{\boldsymbol{\varepsilon}}=\begin{bmatrix}\tilde{\varepsilon}_H & 0 & 0\\ 0 & \tilde{\varepsilon}_H & 0\\ 0 & 0 & \tilde{\varepsilon}_V\end{bmatrix}=\begin{bmatrix}\varepsilon_H+i\frac{\sigma_H}{\omega} & 0 & 0\\ 0 & \varepsilon_H+i\frac{\sigma_H}{\omega} & 0\\ 0 & 0 & \varepsilon_V+i\frac{\sigma_V}{\omega}\end{bmatrix}. \tag{A-6}$$

The horizontal resistivity is $\rho_H=1/\sigma_H$, and the vertical resistivity is $\rho_V=1/\sigma_V$. The symmetric submatrices $\mathbf{A}_1$ and $\mathbf{A}_2$ are

$$\mathbf{A}_1=-\frac{1}{\tilde{\varepsilon}_V}\begin{bmatrix}\mu_0\tilde{\varepsilon}_V-p_x^2 & -p_xp_y\\ -p_xp_y & \mu_0\tilde{\varepsilon}_V-p_y^2\end{bmatrix} \tag{A-7}$$

and

$$\mathbf{A}_2=-\frac{1}{\mu_0}\begin{bmatrix}\mu_0\tilde{\varepsilon}_H-p_y^2 & p_xp_y\\ p_xp_y & \mu_0\tilde{\varepsilon}_H-p_x^2\end{bmatrix}. \tag{A-8}$$

As demonstrated by Løseth and Ursin (2007), the eigenvalues for the system matrix $\mathbf{A}$ are

$$\lambda_1=-\lambda_3=-s_1\quad\lambda_2=-\lambda_4=-s_2, \tag{A-9}$$

with

$$s_1 = \sqrt{\mu_0\tilde{\epsilon}_h - p^2}, \quad s_2 = \sqrt{\mu_0\tilde{\epsilon}_h - \frac{\tilde{\epsilon}_H}{\tilde{\epsilon}_V}p^2}. \tag{A-10}$$

The eigenvalues λ_1 and λ_3 are for the transverse electric mode, and the eigenvalues λ_2 and λ_4 are for the transverse magnetic mode.

Here we note that the two sets of eigenvalues become equal for vertically propagating fields, that is, for $p_x = p_y = 0$. It is also apparent that the eigenvalues become independent of the vertical permittivity and resistivity for vertically propagating fields. Further on, for the case of vertically propagating fields in a TIV medium, we can use the same composition and decomposition matrices as in Amundsen et al. (2006). The reason is that the structure of the above eigenvalue set becomes identical to the structure found in Amundsen et al. (2006) for vertically propagating fields. Using the decomposition matrix from Amundsen et al. (2006), we find for vertically propagating fields,

$$\begin{aligned} E_x^U &= \frac{1}{2}[E_x - Z_H H_y], \\ E_y^U &= \frac{1}{2}[E_y + Z_H H_x], \\ E_x^D &= \frac{1}{2}[E_x + Z_H H_y], \\ E_y^D &= \frac{1}{2}[E_y - Z_H H_x], \end{aligned} \tag{A-11}$$

where $Z_H = \sqrt{-i\mu_0\omega\rho_H}$ in the quasi-static limit.

The proposed procedure for top-formation resistivity estimation has been tested on synthetic data generated for resistivity models that had large differences between horizontal and vertical resistivity. This anisotropy was also present in the top formation. In all cases, the horizontal resistivity was retrieved. The proposed top-formation resistivity estimation method has no sensitivity to the vertical resistivity. This is a consequence of the selection criteria for offset range and frequency range used for the estimation.

APPENDIX B

THE TOP FORMATION RESISTIVITY

We assume vertically propagating fields in the derivations that follows. The electric-field reflection (r_{ab}) and transmission (t_{ab}) coefficients for media a and b in terms of resistivities are then

$$r_{ab} = \frac{\sqrt{\rho_b} - \sqrt{\rho_a}}{\sqrt{\rho_b} + \sqrt{\rho_a}}, \quad t_{ab} = \frac{2\sqrt{\rho_b}}{\sqrt{\rho_b} + \sqrt{\rho_a}}, \tag{B-1}$$

where the subscript a indicates the medium properties on the side of the interface where the incoming and reflected fields are located and subscript b indicates medium properties on the side of the interface where the transmitted field is found. Seen from the opposite side of the boundary, the reflection coefficients change sign; that is, $r_{ba} = -r_{ab}$. The reflection and transmission coefficients in equation B-1 are in terms of characteristic impedances,

$$r_{ab} = \frac{Z_b - Z_a}{Z_b + Z_a}, \quad t_{ab} = \frac{2Z_b}{Z_b + Z_a}. \tag{B-2}$$

The upgoing electric field in the water layer $E_x^{U,w}(\mathbf{x}_r, \omega|\mathbf{x}_s)$ is the sum of the upgoing electric field in the formation $E_x^{U,f}(\mathbf{x}_r, \omega|\mathbf{x}_s)$ transmitted from the top formation to the seawater plus the reflection of the downgoing field at the seabed, $E_x^{D,w}(\mathbf{x}_r, \omega|\mathbf{x}_s)$,

$$E_x^{U,w}(\mathbf{x}_r, \omega|\mathbf{x}_s) = t_{fw}E_x^{U,f}(\mathbf{x}_r, \omega|\mathbf{x}_s) + r_{wf}E_x^{D,w}(\mathbf{x}_r, \omega|\mathbf{x}_s). \tag{B-3}$$

To demonstrate the relation between the upgoing fields above and below the seabed, we rewrite equation B-3,

$$t_{fw}E_x^{U,f}(\mathbf{x}_r, \omega|\mathbf{x}_s) = E_x^{U,w}(\mathbf{x}_r, \omega|\mathbf{x}_s) - r_{wf}E_x^{D,w}(\mathbf{x}_r, \omega|\mathbf{x}_s), \tag{B-4}$$

or with equation B-1,

$$\begin{aligned} 2\sqrt{\rho_w}E_x^{U,f}(\mathbf{x}_r, \omega|\mathbf{x}_s) = &\left(\sqrt{\rho_f} + \sqrt{\rho_w}\right)E_x^{U,w}(\mathbf{x}_r, \omega|\mathbf{x}_s) \\ &- \left(\sqrt{\rho_f} - \sqrt{\rho_w}\right)E_x^{D,w}(\mathbf{x}_r, \omega|\mathbf{x}_s), \end{aligned} \tag{B-5}$$

which reduces to

$$\begin{aligned} E_x^{U,f}(\mathbf{x}_r, \omega|\mathbf{x}_s) = \frac{1}{2}[&E_x^{D,w}(\mathbf{x}_r, \omega|\mathbf{x}_s) + E_x^{U,w}(\mathbf{x}_r, \omega|\mathbf{x}_s) \\ &- \frac{\sqrt{\rho_f}}{\sqrt{\rho_w}}(E_x^{D,w}(\mathbf{x}_r, \omega|\mathbf{x}_s) - E_x^{U,w}(\mathbf{x}_r, \omega|\mathbf{x}_s))], \end{aligned} \tag{B-6}$$

where the upgoing field below the seabed now is expressed as a function of the upgoing and downgoing fields above the seabed. Equation 1 can be recast as

$$\begin{aligned} E_x^{D,w}(\mathbf{x}_r, \omega|\mathbf{x}_s) + E_x^{U,w}(\mathbf{x}_r, \omega|\mathbf{x}_s) &= E_x(\mathbf{x}_r, \omega|\mathbf{x}_s), \\ E_x^{D,w}(\mathbf{x}_r, \omega|\mathbf{x}_s) - E_x^{U,w}(\mathbf{x}_r, \omega|\mathbf{x}_s) &= Z_w H_y(\mathbf{x}_r, \omega|\mathbf{x}_s), \end{aligned} \tag{B-7}$$

and by using $Z_f = (\sqrt{\rho_f}/\sqrt{\rho_w})Z_w$, it follows from equations B-6 and B-7 that

$$E_x^{U,f}(\mathbf{x}_r, \omega|\mathbf{x}_r) = \frac{1}{2}(E_x(\mathbf{x}_r, \omega|\mathbf{x}_s) - Z_f H_y(\mathbf{x}_r, \omega|\mathbf{x}_s)). \tag{B-8}$$

This demonstrates the consistency between equation 1 and equation B-1 and the effect of the choice of the resistivity used to calculate the characteristic impedance.

The earth's reflectivity as seen from the water layer can be defined as the upgoing field in the water layer divided by the downgoing field in the water layer,

$$R_E(\mathbf{x}_r, \omega|\mathbf{x}_s) = \frac{E_x^{U,w}(\mathbf{x}_r, \omega|\mathbf{x}_s)}{E_x^{D,w}(\mathbf{x}_r, \omega|\mathbf{x}_s)}, \tag{B-9}$$

or with equation 1 and the characteristic impedance of seawater, which is the proper choice when the subsurface is viewed from immediately above the seabed:

$$R_E(\mathbf{x}_r,\omega|\mathbf{x}_s)=\frac{E_x(\mathbf{x}_r,\omega|\mathbf{x}_s)-Z_wH_y(\mathbf{x}_r,\omega|\mathbf{x}_s)}{E_x(\mathbf{x}_r,\omega|\mathbf{x}_s)+Z_wH_y(\mathbf{x}_r,\omega|\mathbf{x}_s)}. \quad \text{(B-10)}$$

Equation B-10 shows that R_E depends on quantities that are directly measured in a marine CSEM survey in which the resistivity of seawater is a standard measurement.

Equation B-10 can be recast as

$$R_E(\mathbf{x}_r,\omega|\mathbf{x}_s)=\frac{Z_{xy}(\mathbf{x}_r,\omega|\mathbf{x}_s)-Z_w}{Z_{xy}(\mathbf{x}_r,\omega|\mathbf{x}_s)+Z_w}, \quad \text{(B-11)}$$

where Z_{xy} is a component of the impedance tensor as it is defined for MT processing under the assumption that the subsurface has a well-defined strike direction (2D medium):

$$Z_{xy}(\mathbf{x}_r,\omega|\mathbf{x}_s)=\frac{E_x(\mathbf{x}_r,\omega|\mathbf{x}_s)}{H_y(\mathbf{x}_r,\omega|\mathbf{x}_s)}. \quad \text{(B-12)}$$

The difference from MT is that the above impedance depends on the lateral source-receiver offset.

A key assumption here is that R_E approaches the seabed zero-incidence-angle reflection coefficient at sufficiently large source-receiver offsets as the frequency approaches a limiting high frequency ω_l. The argument is that as the frequency increases, the skin depth becomes smaller, and hence, the electromagnetic field becomes insensitive to deeper layers in the formation and mainly sensitive to resistivity variations at the seabed. For any choice of the frequency ω_l, we have to require that the source-receiver separation is sufficiently large so that the vertically propagating field assumption is valid. It is well known that the signal-to-noise ratio becomes smaller with increased frequency, mainly because field amplitudes at higher frequencies are heavily damped in a diffusive medium. This put an upper limit on ω_l. An estimate of ω_l is needed, and for practical applications of the proposed scheme it is necessary that the electric and magnetic fields have amplitudes above the noise level for ω_l. Hence, the two main guiding principles for choosing ω_l are that it is sufficiently high so that the vertical propagation assumption is valid over a large offset range, including relatively small offsets, and on the other hand that it is sufficiently low so that the electromagnetic fields are above the noise level.

We assume that a proper ω_l can be found. In which case we have that $Z_{xy}(\mathbf{x}_r,\omega|\mathbf{x}_s)$ approaches a half-space value, which at high frequencies is the top-formation characteristic impedance (Vozoff, 1991). Thus,

$$R_E(\mathbf{x}_r,\omega|\mathbf{x}_s)|_{\omega\to\omega_l}\approx\frac{\sqrt{\rho_f}-\sqrt{\rho_w}}{\sqrt{\rho_f}+\sqrt{\rho_w}}, \quad \text{(B-13)}$$

which gives

$$\sqrt{\rho_f}(1-R_E(\mathbf{x}_r,\omega_l|\mathbf{x}_s))=\sqrt{\rho_w}(1+R_E(\mathbf{x}_r,\omega_l|\mathbf{x}_s)), \quad \text{(B-14)}$$

and using equation B-11,

$$\sqrt{\rho_f}=\sqrt{\rho_w}\frac{Z_{xy}(\mathbf{x}_r,\omega_l|\mathbf{x}_s)}{Z_w}. \quad \text{(B-15)}$$

The square root of the resistivity of seawater is in the numerator and denominator, so equation B-15 gives

$$\rho_f(\mathbf{x}_r,\omega_l|\mathbf{x}_s)=\frac{|Z_{xy}(\mathbf{x}_r,\omega_l|\mathbf{x}_s)|^2}{\mu_0\omega}, \quad \text{(B-16)}$$

which is similar to the expression for the apparent resistivity in MT processing under the assumption that the subsurface has a well-defined strike direction. Again, the difference is that the expression in equation B-16 formally depends on the lateral source-receiver offset. We will show in the Results section that for the proper choice of ω_l, $\rho_f(\mathbf{x}_r,\omega_l|\mathbf{x}_s)$ becomes close to constant as a function of source-receiver offsets and at approximately the true top-formation resistivity value, if the offsets are sufficiently large.

No attempt at averaging is done yet. We will use the criterion of constant $\rho_f(\mathbf{x}_r,\omega_l|\mathbf{x}_s)$ with source-receiver offset to set the offset range used for average estimates of the top-formation resistivity. The practical implication is that we use data that are dominated by the airwave for the estimation of the top-formation resistivity. The airwave shares the property with the incoming MT field that the Poynting vector is close to the vertical axis. Viewed from the receiver position, the airwave due to a sufficiently distant transmitter can be approximated by a vertically propagating plane wave. The formation resistivity function in equation B-16 is formally a function of the parameter vector of the survey $[\mathbf{x}_r,\omega_l,\mathbf{x}_s]^T$. Real data are noisy, and we need a stable estimate for the top-formation resistivity for each receiver $\langle\rho_f(\mathbf{x}_r)\rangle$. We choose

$$\langle\rho_f(\mathbf{x}_r)\rangle=\frac{1}{N_s}\sum_{\omega_l}\sum_{\mathbf{x}_s=\mathbf{x}_a(\omega_l)}^{\mathbf{x}_b(\omega_l)}\rho_f(\mathbf{x}_r,\omega_l|\mathbf{x}_s), \quad \text{(B-17)}$$

where the sum over ω_l is a sum over a group of frequencies or a single frequency that has the property that field amplitudes are above the noise level at sufficiently large offsets and that the fields at these frequencies are mostly sensitive to the resistivity contrast between the seawater and the top formation. The sum over $\mathbf{x}_s$ is for a range of source-receiver offset $[\mathbf{x}_a(\omega_l),\mathbf{x}_b(\omega_l)]$, where the lower bound $\mathbf{x}_a(\omega_l)$ must be sufficiently large to give a dominant airwave contribution in the downgoing field. These are the offsets in which the CSEM fields are most similar to MT fields and in which the formation-resistivity function of equation B-16 becomes insensitive to the source location. The range $[\mathbf{x}_a(\omega_l),\mathbf{x}_b(\omega_l)]$ is frequency dependent. The normalization factor N_s equals the number of samples in the sum.

The upgoing field below the seabed can now be expressed:

$$E_x^U(\mathbf{x}_r,\omega|\mathbf{x}_s)=\frac{1}{2}(E_x(\mathbf{x}_r,\omega|\mathbf{x}_s)-Z_f(\mathbf{x}_r)H_y(\mathbf{x}_r,\omega|\mathbf{x}_s)), \quad \text{(B-18)}$$

with

$$Z_f(\mathbf{x}_r)=\sqrt{-i\mu_0\omega\langle\rho_f(\mathbf{x}_r)\rangle}. \quad \text{(B-19)}$$

REFERENCES

Abubakar, A., T. M. Habashy, V. L. Druskin, L. Knizhnerman, and D. Alumbaugh, 2008, 2.5D forward and inverse modeling for interpreting low-frequency electromagnetic measurements: Geophysics, **73**, no. 4, F165–F177, doi: 10.1190/1.2937466.

Amundsen, L., L. Løseth, R. Mittet, S. Ellingsrud, and B. Ursin, 2006, Decomposition of electromagnetic fields into upgoing and downgoing components: Geophysics, **71**, no. 5, G211–G223, doi: 10.1190/1.2245468.

Andréis, D., and L. M. MacGregor, 2008, Controlled-source electromagnetic sounding in shallow water: Principles and applications: Geophysics, **73**, no. 1, F21–F32, doi: 10.1190/1.2815721.

Andréis, D., L. M. MacGregor, and N. Golubev, 2009, Electromagnetic surveying: U. S. Patent, 7,565,245 B2.

Chen, J., and D. L. Alumbaugh, 2011, Three methods for mitigating airwaves in shallow water marine controlled-source electromagentic data: Geophysics, **76**, no. 2, F89–F99, doi: 10.1190/1.3536641.

Constable, S., 2010, Ten years of marine CSEM for hydrocarbon exploration: Geophysics, **75**, no. 5, A67–A81, doi: 10.1190/1.3483451.

Eidesmo, T., S. Ellingsrud, L. M. MacGregor, S. Constable, M. C. Sinha, S. Johansen, F. N. Kong, and H. Westerdahl, 2002, Sea bed logging (SBL), a new method for remote and direct identification of hydrocarbon filled layers in deepwater areas: First Break, **20**, 144–152.

Ellingsrud, S., T. Eidesmo, M. C. Sinha, L. M. MacGregor, and S. Constable, 2002, Remote sensing of hydrocarbon layers by seabed logging (SBL): Results from a cruise offshore Angola: The Leading Edge, **21**, 972–982, doi: 10.1190/1.1518433.

Hansen, K. R., and R. Mittet, 2009, Incorporating seismic horizons in inversion of CSEM data: 79th Annual International Meeting, SEG, Expanded Abstracts, 694–698.

Johansen, S. E., H. E. F. Amundsen, T. Røsten, S. Ellingsrud, T. Eidesmo, and A. H. Bhuyian, 2005, Subsurface hydrocarbons detected by electromagnetic sounding: First Break, **23**, 31–36, doi: 10.3997/1365-2397.2005005.

Key, K., 2009, 1D inversion of multicomponent, multifrequency marine CSEM data: Methodology and synthetic studies for resolving thin resistive layers: Geophysics, **74**, no. 2, F9–F20, doi: 10.1190/1.3058434.

Lee, K. H., G. Liu, and H. F. Morrison, 1989, A new approach to modeling the electromagnetic response of conductive media: Geophysics, **54**, 1180–1192, doi: 10.1190/1.1442753.

Løseth, L. O., and B. Ursin, 2007, Electromagnetic fields in planarly layered anisotropic media: Geophysical Journal International, **170**, 44–80, doi: 10.1111/gji.2007.170.issue-1.

Maaø, F. A., 2007, Fast finite-difference time-domain modeling for marine-subsurface electromagnetic problems: Geophysics, **72**, no. 2, A19–A23, doi: 10.1190/1.2434781.

Mittet, R., 2008, Normalized amplitude ratios for frequency-domain CSEM in very shallow water: First Break, **26**, 47–54, doi: 10.3997/1365-2397.2008016.

Mittet, R., 2010, High-order finite-difference simulations of marine CSEM surveys using a correspondence principle for wave and diffusion fields: Geophysics, **75**, no. 1, F33–F50, doi: 10.1190/1.3278525.

Mittet, R., K. Brauti, H. Maulana, and T. A. Wicklund, 2008, CMP inversion and post-inversion modelling for marine CSEM data: First Break, **26**, 59–67, doi: 10.3997/1365-2397.2008011.

Mittet, R., and T. Schaug-Pettersen, 2008, Shaping optimal transmitter waveforms for marine CSEM surveys: Geophysics, **73**, no. 3, F97–F104, doi: 10.1190/1.2898410.

Nordskag, J. I., and L. Amundsen, 2007, Asymptotic airwave modeling for marine controlled-source electromagnetic surveying: Geophysics, **72**, no. 6, F249–F255, doi: 10.1190/1.2786025.

Ou, S., D. Willen, and D. Pavlov, 2011, Equivalence of controlled-source electric and magnetic data for resistivity inversion: 81st Annual International Meeting, SEG, Expanded Abstracts, 578–582.

Roth, F., and J. J. Zach, 2007, Inversion of marine CSEM data using up-down wavefield separation and simulated annealing: 77th Annual International Meeting, SEG, Expanded Abstracts, 524–528.

Vozoff, K., 1991, The magnetotelluric method, *in* M. N. Nabighian, ed., Electromagnetic methods in applied geophysics — Applications: SEG, 641–711.

Zonge, K. L., and L. J. Hughes, 1991, Controlled source audio-frequency magnetotellurics, *in* M. N. Nabighian, ed., Electromagnetic methods in applied geophysics — Applications: SEG, 713–809.